Ultrastructure and surface composition of glutathione-terminated ultrasmall silver, gold, platinum and alloyed silver-platinum nanoparticles (2 nm)

by

Natalie Wolff,[1] Kateryna Loza,[1] Marc Heggen,[2] Torsten Schaller,[3] Felix Niemeyer,[3] Peter Bayer,[4] Christine Beuck,[4] Cristiano L. P. Oliveira,[5] Oleg Prymak,[1] Claudia Weidenthaler,[6] and Matthias Epple[1,*]

[1] Inorganic Chemistry and Centre for Nanointegration Duisburg-Essen (CENIDE), University of Duisburg-Essen, 45117 Essen, Germany

[2] Ernst-Ruska Centre for Microscopy and Spectroscopy with Electrons, Forschungszentrum Jülich GmbH, 52428 Jülich, Germany

[3] Organic Chemistry, University of Duisburg-Essen, 45117 Essen, Germany

[4] Structural and Medicinal Biochemistry, University of Duisburg-Essen, 45117 Essen, Germany

[5] Institute of Physics, University of São Paulo, São Paulo 05508-090, Brazil

[6] Max-Planck-Institut für Kohlenforschung, Kaiser-Wilhelm-Platz 1, 45470 Mülheim an der Ruhr, Germany

* Author for correspondence: matthias.epple@uni-due.de

Abstract

Alloyed ultrasmall silver-platinum nanoparticles (Ag:Pt = 50:50) were prepared and compared to pure silver, platinum, and gold nanoparticles, all with a diameter of 2 nm. They were surface-stabilized by a layer of glutathione (GSH). A comprehensive characterization by high-resolution transmission electron microscopy (HRTEM),

electron diffraction (ED), X-ray diffraction (XRD), small-angle X-ray scattering (SAXS), differential centrifugal sedimentation (DCS), and UV spectroscopy showed their size both in the dry and in the water-dispersed state (hydrodynamic diameter). Solution NMR spectroscopy (^{1}H, ^{13}C, COSY, HSQC, HMBC, DOSY) showed the nature of the glutathione shell including the number of GSH ligands on each nanoparticle (about 200 with a molecular footprint of 0.063 nm^2 each). It furthermore showed that there are at least two different positions for the GSH ligand on the gold nanoparticle surface. Platinum strongly reduced the resolution of the NMR spectra compared to silver and gold, also in the alloyed nanoparticles. X-ray photoelectron spectroscopy (XPS) showed that silver, platinum, and silver-platinum particles were at least partially oxidized to Ag(+I) and Pt(+II) whereas the gold nanoparticles showed no sign of oxidation. Platinum and gold nanoparticles were well crystalline but twinned (fcc lattice) despite the small particle size. Silver was crystalline in electron diffraction but not in X-ray diffraction. Alloyed silver-platinum nanoparticles were almost fully amorphous by both methods, indicating a considerable internal disorder.

Keywords

Nanoparticles; silver; platinum; gold; nanoalloys

Introduction

The properties of alloyed nanoparticles can be easily varied by changing their composition.[1-6] Thus, they are of considerable interest in heterogeneous catalysis,[7-14] imaging,[15, 16] and sensing.[16, 17] If the particles are very small, i.e. smaller than about 3 nm, they enter the regime of ultrasmall nanoparticles[18] approaching atom-sharp metal clusters with defined structure and stoichiometry. Such nanoparticles consist of only a few hundred atoms.[19-27] As they are so small, they are interesting objects in

biomedical studies as they may penetrate biological barriers like nuclear membranes[28, 29] and the blood-brain barrier.[30] They can also be used to fine-tune the interaction with biomolecules in biological media (e.g. when forming the so-called protein corona).[31-34] Ultrasmall gold nanoparticles have been extensively studied, also with respect to their structure and ligand shell composition,[24, 26, 35-38] but other metals and alloyed ultrasmall nanoparticles have been much less explored with respect to structure and ligand shell.

Here we report a comprehensive study on alloyed silver-platinum nanoparticles with a molar ratio of 1:1, stabilized by the capping ligand glutathione. Their water-based synthesis is presented as well as a detailed characterization with respect to size, structure, and ligand shell composition. The advantages of a water-based synthesis are an easy dispersability in water and the option to prepare several tens of milligrams in one batch. For comparison, the monometallic nanoparticles of silver, platinum, and gold were prepared and characterized in the same way. While ultrasmall gold nanoparticles are understood as a general model system, the comparison of the pure metals silver and platinum with alloyed ultrasmall nanoparticles sheds light on the peculiarities of an ultrasmall nanoalloy.

Results and discussion

Ultrasmall nanoparticles of silver, gold, platinum, and silver-platinum were prepared by reduction of the corresponding metal salts with $NaBH_4$ in modified Brust-Schiffrin syntheses.[39, 40] The well-established tripeptide glutathione served as capping agent of the water-dispersed nanoparticles.[41-43] The molar metal ratio in the bimetallic AgPt nanoparticles was close to 1:1 as shown by elemental analysis (see below).

Figure 1 shows HRTEM images of ultrasmall nanoparticles. The core diameter was assessed by measuring the dimensions of at least 100 particles from different

HRTEM images. The average particle diameter was between 1.5 and 2.5 nm with a narrow particle size distribution. Electron diffraction, accompanied by Fast Fourier transformation (FFT) of single particles showed the internal crystallinity (Figure 2). Silver, platinum and gold nanoparticles showed a high degree of crystallinity, and the measured unit cell parameters were in a good agreement with the literature. In contrast, no crystalline fringes were detected for bimetallic AgPt nanoparticles, indicating that their internal structure was associated with considerable disorder.

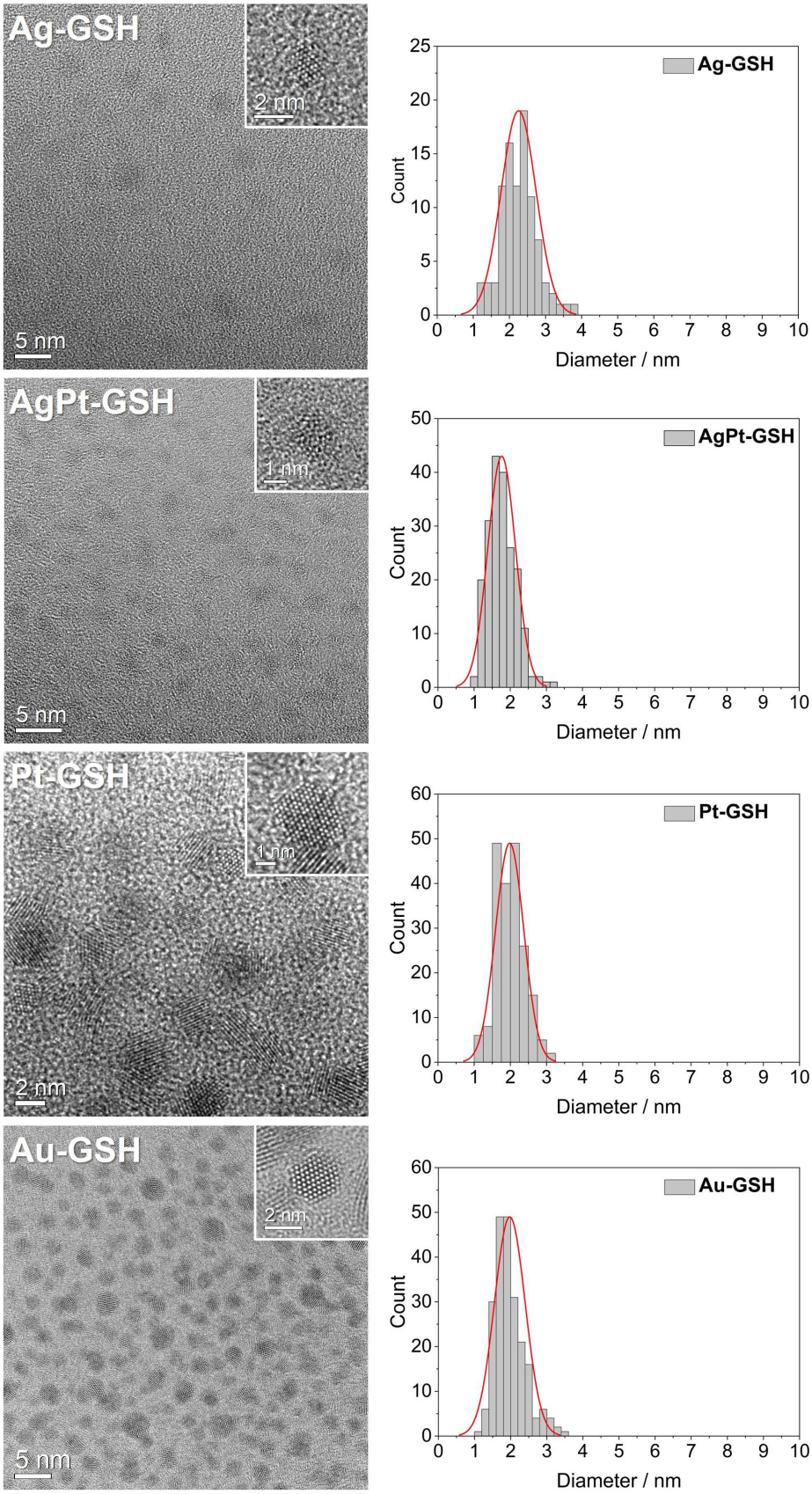
Ag-GSH
2 nm
5 nm
Ag-GSH
Count
Diameter / nm
AgPt-GSH
1 nm
5 nm
AgPt-GSH
Count
Diameter / nm
Pt-GSH
1 nm
2 nm
Pt-GSH
Count
Diameter / nm
Au-GSH
2 nm
5 nm
Au-GSH
Count
Diameter / nm

Figure 1: HRTEM images of GSH-stabilized monometallic silver, platinum, gold, and alloyed silver-platinum nanoparticles, together with particle size distributions.

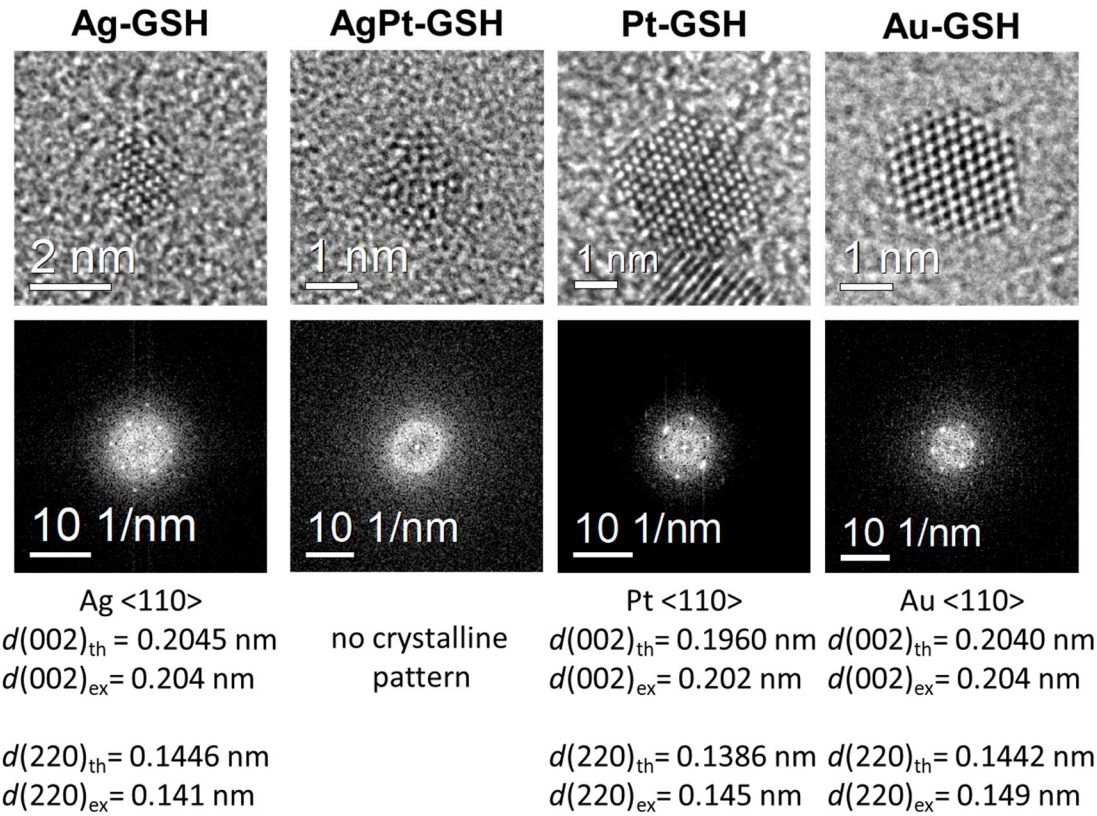

Figure 2. HRTEM images of individual ultrasmall nanoparticles and corresponding FFT patterns with theoretical (th) and experimental (ex) *d*-spacings. The images for silver, platinum, and gold nanoparticles were obtained along a low-index zone axis orientation (110). Silver, gold, and platinum nanoparticles showed a high crystallinity of the fcc lattice whereas alloyed silver-platinum nanoparticles (50:50) had a highly disordered structure.

As complementary method, small-angle X-ray scattering (SAXS) provides the diameter of the metallic core in dispersion, including information on particle agglomeration. Model fits and obtained sizes distributions are given in Figure 3 and Table 1.

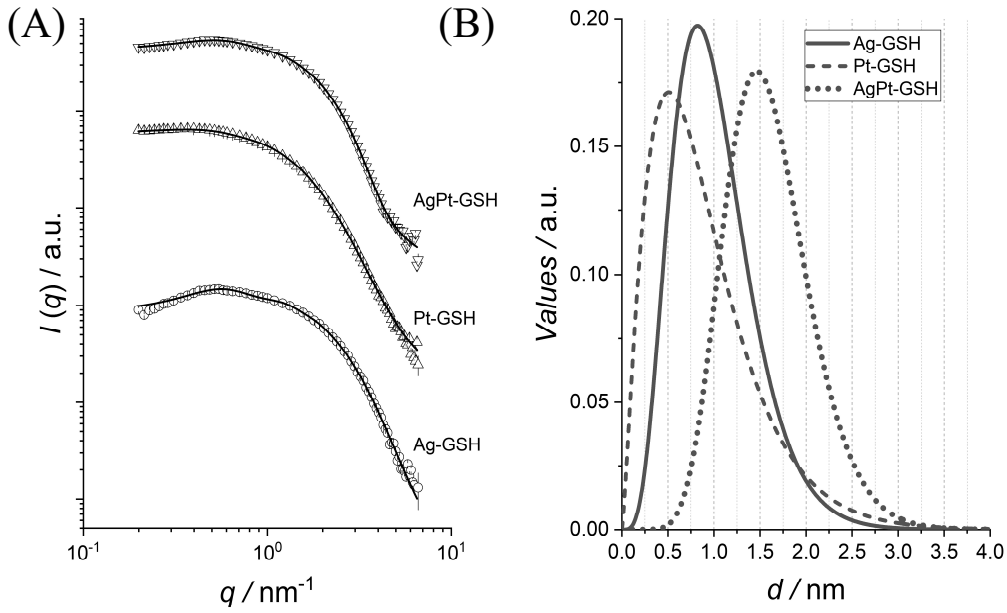

Figure 3: SAXS data and modeling results of water-dispersed Ag-GSH, Pt-GSH, and AgPt-GSH nanoparticles. **A**: Experimental data (symbols) and theoretical fits (solid curves). The curves were shifted for clarity. **B**: Particle size distributions

Table 1: Numerical results of the SAXS evaluation of water-dispersed nanoparticles. Standard deviations of the last digits given in parentheses.

	Ag-GSH	AgPt-GSH	Pt-GSH
Sc_1	0.151(1)	0.572(1)	0.689(3)
$d = 2 \cdot R_o$ / nm	1.02(6)	1.60(14)	0.88(10)
σ / nm	0.22(1)	0.23(2)	0.29(6)
R_{HS} / nm	4.9(4)	4.8(1)	6(1)
η	0.071(4)	0.036(2)	0.020(6)

The scale factors are directly related to concentration, contrasts and average volume square of the particles in the system. With respect to the particle sizes, the modeling

indicated that the silver and platinum nanoparticles were smaller (about 1 nm) than the silver-platinum nanoparticles (1.6 nm). There was no indication of agglomeration. The results for silver-platinum nanoparticles agree well with the HRTEM data. For the silver-platinum nanoparticles, the sizes obtained by SAXS are smaller than the ones obtained by HRTEM. However, the size measured by SAXS is the result of averaging over a very large particle ensemble, i.e. much larger than the number of particles analyzed by TEM. The polydispersities obtained from SAXS analysis were 0.22 nm (43%) for silver, 0.29 nm (65%) for platinum and 0.23 nm (29%) for the silver platinum nanoparticles. This confirms the monomodal particle size distribution from the HRTEM data (Figure 1). The volume fraction of the particles in the system (parameter η) were 7%, 2% and 3.6% for the silver, platinum and silver-platinum nanoparticles, respectively, indicating a relatively low concentration of the particles in the system. An interesting result is the average interaction radius, R_{HS} which gives an indication on the minimum distance between the particles in the system. The obtained values are very large compared to the nanoparticle size and may be related to the molecules attached to the particle surface.

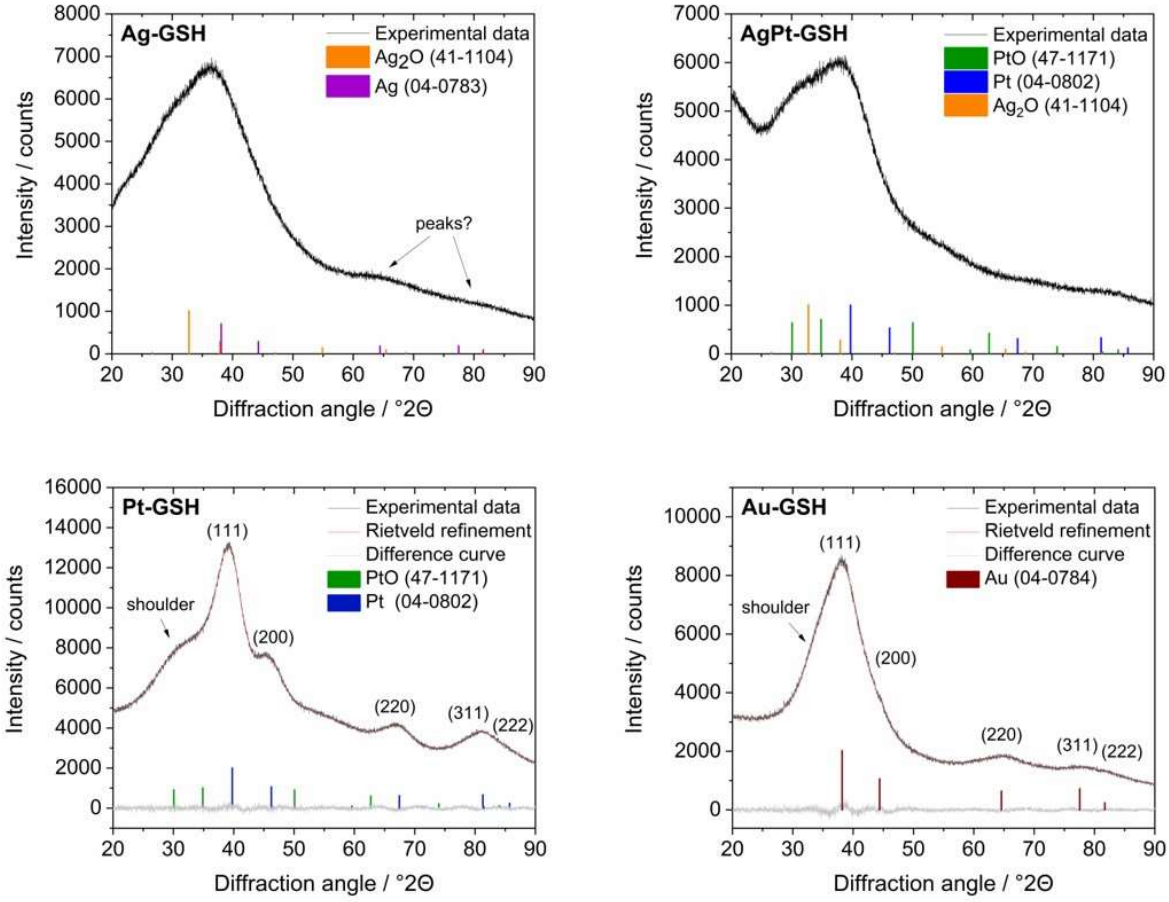

Figure 4. X-ray powder diffractograms of GSH-stabilized silver, silver-platinum, platinum, and gold nanoparticles with qualitative phase analysis and Rietveld refinement. The ICDD numbers in parentheses are given for the corresponding pure phases. The reference peaks of the corresponding oxide phases are shown because there were indications from XPS that silver, silver-platinum, and platinum nanoparticles were at least partially oxidized.

X-ray powder diffraction (XRD) gave very broad diffraction peaks for all types of nanoparticles, confirming their ultrasmall size with small crystalline domains (Figure 4). Platinum and gold clearly showed the diffraction peaks of the fcc lattice, but silver and silver-platinum nanoparticles were either amorphous or contained very small crystallites (significantly below 1 nm) which were not detectable by XRD. The fcc

peak profiles of platinum and gold nanoparticles enabled the determination of their lattice parameters and crystallite sizes by quantitative Rietveld refinement (Table 2).

Table 2: Crystallographic properties of ultrasmall nanoparticles, as determined by X-ray powder diffraction (Rietveld refinement). The crystallite sizes were determined both from the integral broadening (IB) and the full width at half maximum (FWHM).

Sample	**Ag-GSH**	**AgPt-GSH**	**Pt-GSH**	**Au-GSH**
Crystal system / space group	amorphous	amorphous	cubic / Fm-3m	cubic / Fm-3m
Lattice parameter *a* / Å	-	-	*a* = 3.92±0.05	*a* = 4.06±0.08
Crystallite size (IB) / nm	-	-	0.9±1	0.8±1
Crystallite size (FWHM) / nm	-	-	1.3±0.1	1.2±0.1
X-ray density / g cm^3	-	-	21.6±0.8	19.6±0.9

In all cases, the phase analysis was challenging because of the very broad diffraction peaks. The calculated crystallite sizes of platinum and gold nanoparticles were smaller than the TEM diameters of these particles, indicating a polycrystalline (twinned) nature, in agreement with earlier results.[44-47] There was no indication for another phase in the case of gold, but platinum appeared to be partially oxidized to PtO. To elucidate the oxidation state of the metals in the nanoparticles, X-ray photoelectron spectroscopy (XPS) was applied (Figure 5).

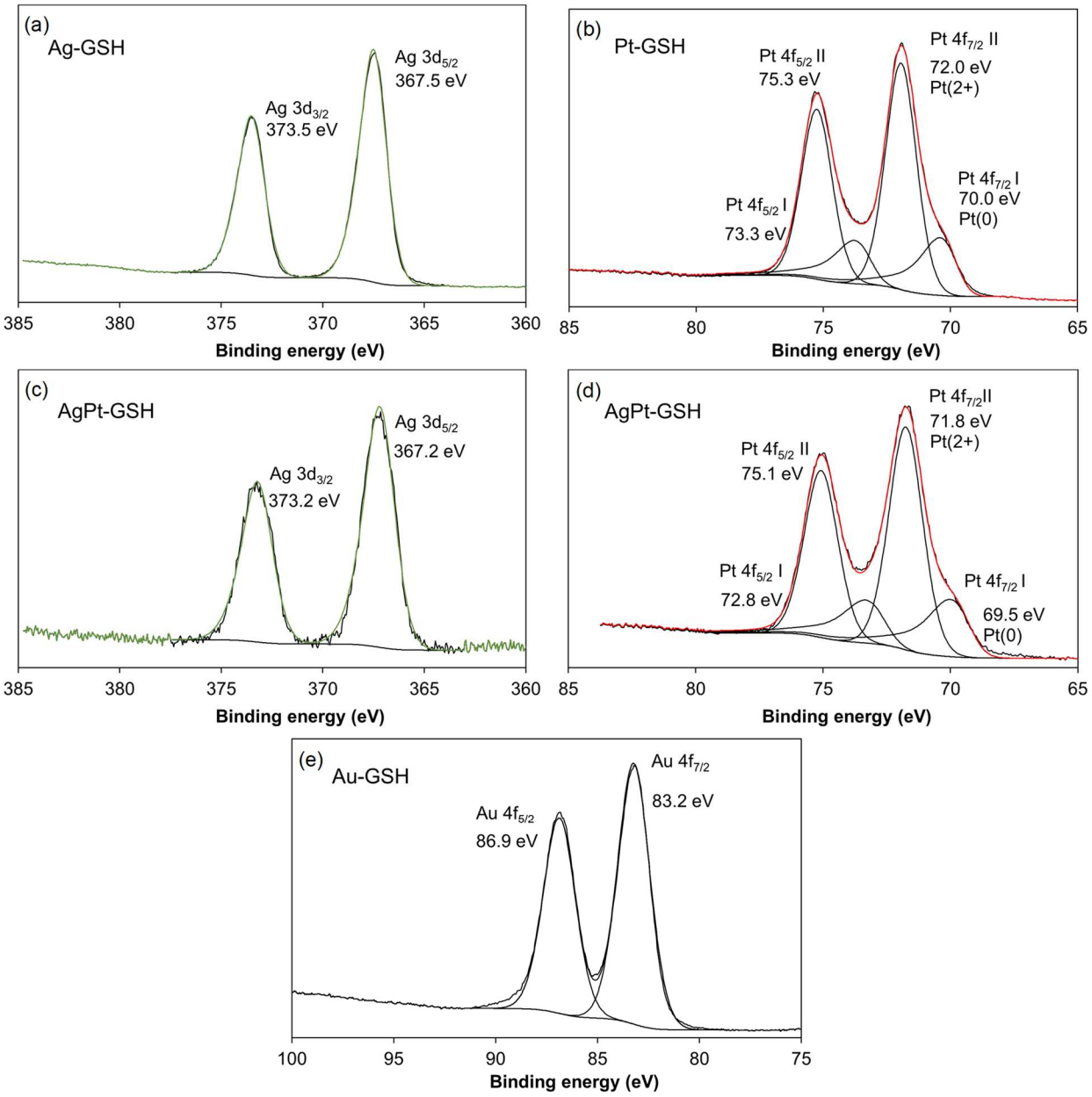

Figure 5: Core electron XP spectra of (a) Ag-GSH, (b) Pt-GSH, (c) AgPt-GSH Ag 3d spectrum, (d) AgPt-GSH Pt 4f spectrum, and (e) Au-GSH nanoparticles.

The analysis of the XP spectra showed that the silver nanoparticles were fully oxidized to Ag_2O, which was confirmed by the analysis of the binding energy value of 367.5 eV in combination with the calculation of the Auger parameter of 724.1 eV. The silver spectrum obtained for the AgPt sample was also assigned to oxidized silver. The pure platinum sample contained two species, i.e. Pt(+II) and Pt(0) with

Pt(+II) being the main species, in accordance with the XRD results. This was also observed for platinum in the AgPt alloy, where no information from XRD was available. The gold spectrum showed only elemental Au(0) with a binding energy of 83.2 eV, in accordance with XRD, which is typical for very small Au nanoparticles.[48] For cysteine-coated ultrasmall gold nanoparticles, binding energies of 87.65 and 83.95 eV were reported, with less than 5% of gold being present as Au(+I).[49]

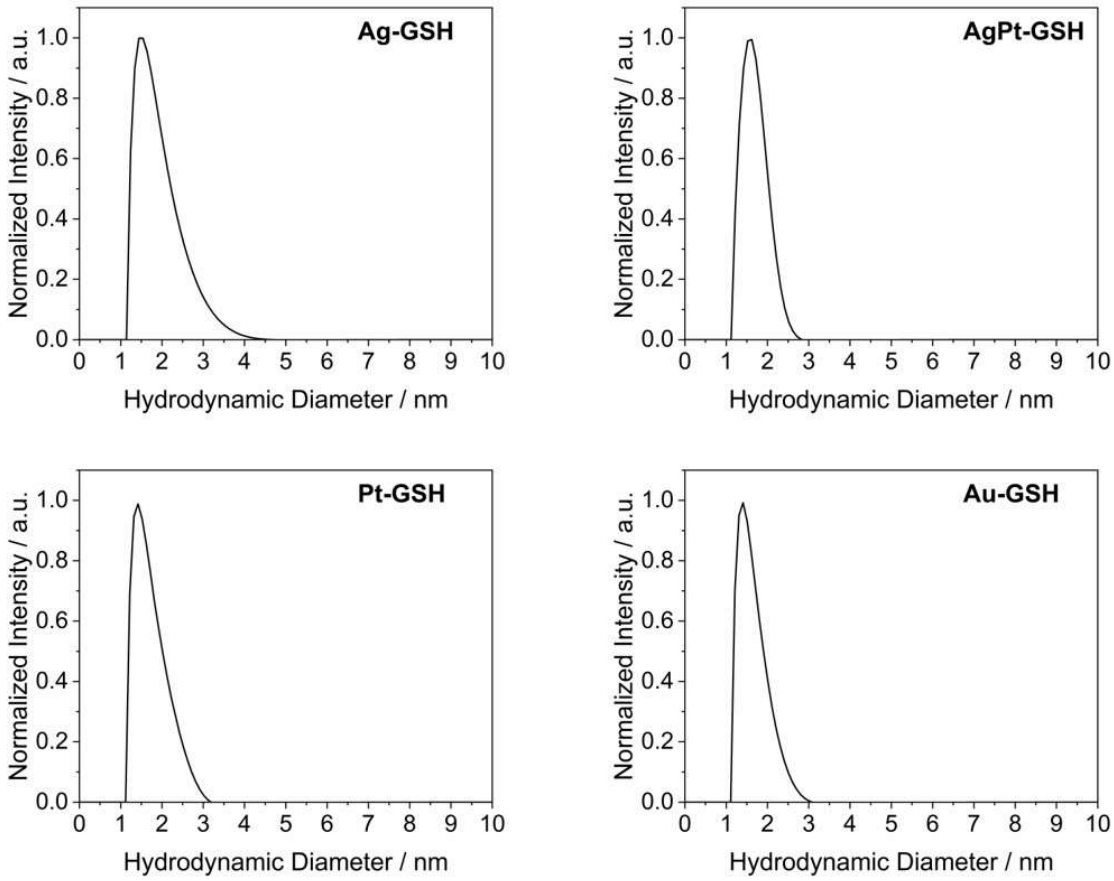

Figure 6. Differential centrifugal sedimentation (DCS) of GSH-stabilised silver, silver-platinum, platinum, and gold nanoparticles. All particles were ultrasmall and well dispersed in water. No aggregates or larger particles were present.

Differential centrifugal sedimentation (DCS) was used to determine the hydrodynamic diameter of the nanoparticles dispersed in water (Figure 6). All

nanoparticle types had a particle diameter below 2 nm. It is important to note that DCS generally underestimates the particle size, as the actual density of the nanoparticles is lower due to the hydrated ligand shell.[50] Thus, the particles appear smaller than their solid core. However, the DCS results agree well with those by TEM and also show an excellent dispersibility of the glutathione-stabilized nanoparticles in water. The particles were too small to give an interpretable signal in dynamic light scattering (DLS) as control experiments showed.

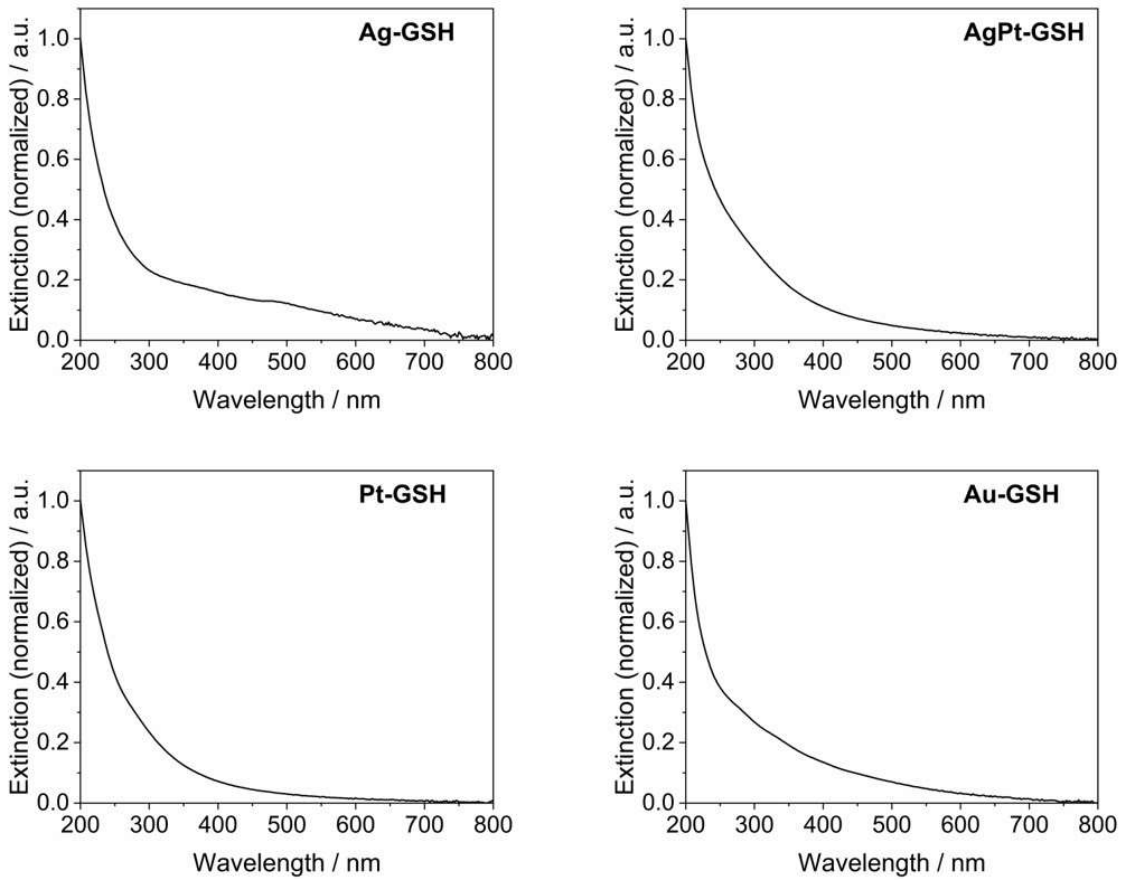

Figure 7. UV-Vis spectra of water-dispersed GSH-stabilised silver, silver-platinum, platinum, and gold nanoparticles.

UV-Vis spectroscopy was used to verify the absence of larger (plasmonic) nanoparticles (Figure 7). Notably, capping agents can change the electronic structure

of nanoparticles and affect surface plasmon resonance by influencing the oscillation frequency of conduction band electrons on the surface of nanoparticles.[51, 52] They can also lead to efficient fluorescence quenching.[53] The surface plasmon resonance (SPR) absorption between 380-420 nm in the UV-Vis spectrum that is characteristic for larger silver nanoparticles was neither present in silver nor in AgPt nanoparticles.[52, 54, 55] The broad absorption plateau around 500 nm for silver nanoparticles has already been reported in the literature.[46, 53, 56] It has been ascribed to an electronic interaction between the ligand and the metal core for PVP-stabilised platinum nanoparticles (8-16 nm).[57] The ultrasmall platinum-containing particles (Pt and AgPt) did not show a plasmon resonance band as known for larger platinum nanoparticles.[56] Small platinum nanoparticles (below 10 nm) show a a very broad absorption in the UV range (below 300 nm).[58, 59] The UV absorption band at 520 nm which is characteristic for plasmonic gold nanoparticles (10 nm and bigger) was not observed.[52, 60] In summary, all nanoparticles presented here showed only an absorption band in the near-UV region but no surface plasmon resonance bands. Therefore we can exclude the presence of larger plasmonic nanoparticles for all particles presented here. None of the particles showed autofluorescence as shown by fluorescence spectroscopy.

Solution NMR spectroscopy on nanoparticles, especially with a diameter larger than 5 nm, often faces problems in spectral resolution due to extreme line broadening. Ultrasmall nanoparticles, however, are small enough to give sufficiently resolved signals in solution NMR spectroscopy,[49, 61-65] providing information about the organic ligand shell. The spectra of all ultrasmall nanoparticles are shown in Figure 8 in comparison with dissolved GSH. In addition, a physical mixture of silver and platinum nanoparticles was investigated.

Even for ultrasmall metallic nanoparticles,[45, 66] the peaks of the ligand glutathione are significantly broadened due to magnetic interactions of the metallic nanoparticle

surface with the proton spins. This effect is stronger near the metallic surface[65] and was observed for both monometallic and bimetallic nanoparticles. However, for silver and gold nanoparticles, the NMR peaks were much narrower than those of platinum and AgPt nanoparticles. In contrast to group 11 metals (silver and gold), platinum in (at least partially) oxidized form as group 10 metal has an open d-shell with unpaired electrons, causing additional paramagnetic line broadening.[45] The spectrum of dissolved GSH permitted a straightforward peak assignment for all nanoparticles. A comparison between the spectra of alloyed AgPt nanoparticles and an equimolar mixture of silver and platinum nanoparticles demonstrates that the AgPt nanoparticles are indeed alloyed whereas the spectrum of the physical mixture is a simple superposition of the spectra of the isolated silver and platinum nanoparticles. The ^{1}H-NMR spectrum also permits to assess the purity of the nanoparticle dispersion. As there were no narrow signals in the NMR spectrum, the presence of residual unbound (i.e. dissolved) glutathione can be excluded.

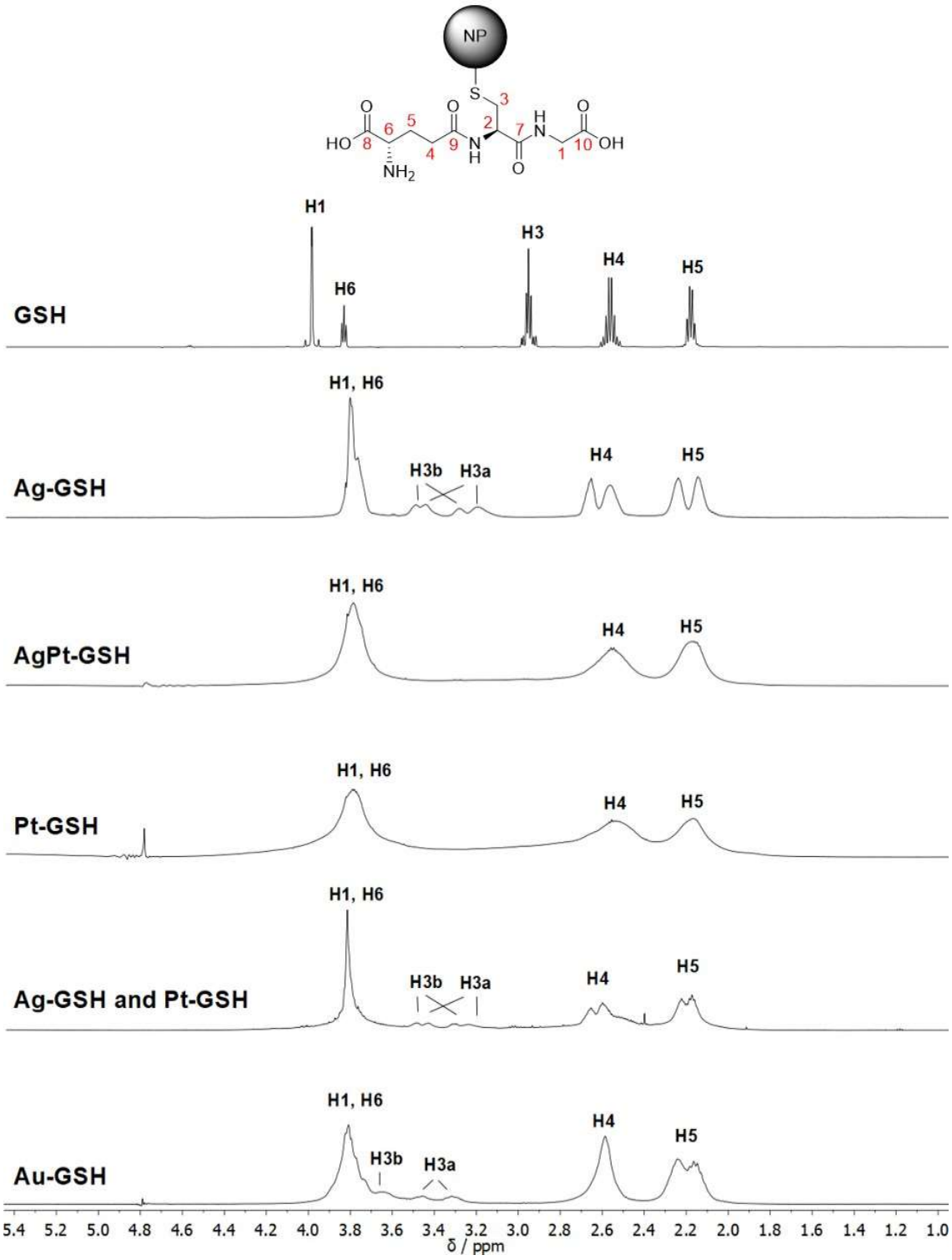

Figure 8: ^{1}H-NMR spectra of GSH-stabilized nanoparticles and unbound GSH (100% D_2O; pH 8.5). The strongly broadened NMR signals are due to the vicinity of the metallic core of the nanoparticles. Notably, the spectra of silver and gold nanoparticles are better resolved than those of platinum and AgPt. The physical

mixture of silver and platinum nanoparticles is a superposition of the spectra of their components.

Because all spectra were measured with simultaneous suppression of the water signal at 4.79 ppm, the H2 signal (at 4.6 ppm for Au-GSH nanoparticles[46]) was not detectable. Most interestingly, in some of the spectra, more than the two expected signals for the diastereotopic H3 protons (β-CH_2 group of glutathione) were observed. The NMR spectrum of the silver nanoparticles showed four well-resolved signals for H3. Three H3 signals (3.64 ppm, 3.46 ppm, 3.31 ppm) were observed for the gold nanoparticles, while for the AgPt and platinum nanoparticles, the H3 protons could not be detected, obviously due to the pronounced line broadening caused by platinum. Additional ^{13}C-NMR, ^{1}H-^{13}C-HSQC and ^{1}H-^{13}C-HMBC spectra were necessary for an unequivocal assignment of the protons.

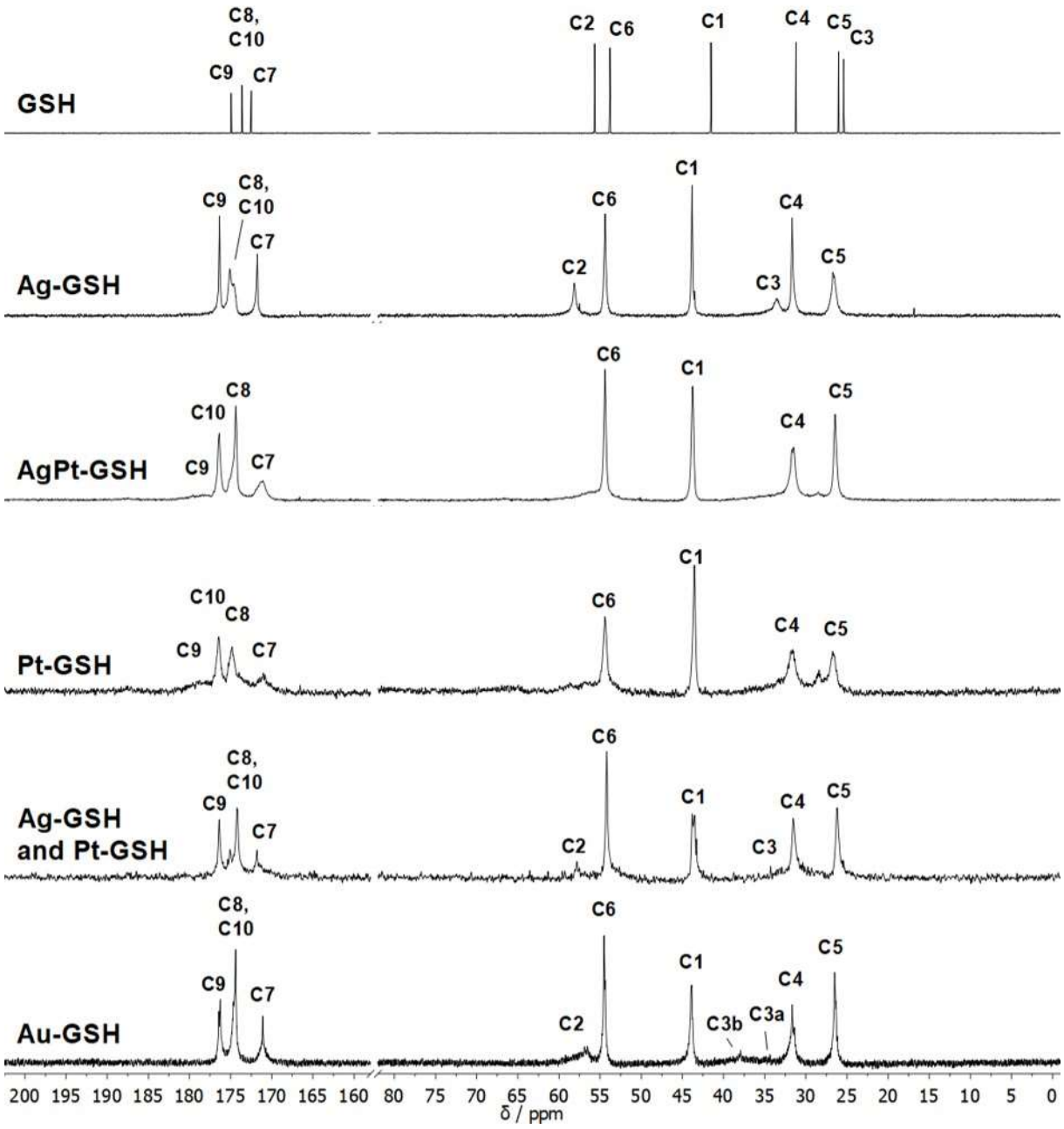

Figure 9: ^{13}C-NMR spectra of GSH-stabilised nanoparticles and dissolved GSH (100% D_2O; pH 8.5). The presence of platinum led to considerable peak broadening. The carbon atoms C2 and C3 close to the metal core were identified in the silver nanoparticles and in the gold nanoparticles as well as in the physical mixture of silver and platinum nanoparticles with the help of ^{1}H-^{13}C-HSQC data.

The ^{13}C-NMR spectra of the GSH-functionalized nanoparticles showed remarkable differences (Figure 9). In the ^{13}C-NMR spectra of silver and gold nanoparticles, the carbon atoms in the C2- and C3-positions in close proximity to the metal core (C2=58.16 ppm; C3=33.58 ppm) were detected with considerably decreased intensity. In contrast, no comparable signals were found for platinum and bimetallic AgPt nanoparticles, only broad shoulders next to the signals of the C4 and C6 carbon atoms. This again highlights again the negative impact of platinum on the resolution of the NMR spectra. Not surprisingly, in the case of the physical mixture of silver and platinum nanoparticles, the signals of C2 and C3 were both present and could be assigned to GSH on silver nanoparticles. The resolution of the spectrum of the gold nanoparticles was comparable to that of the silver nanoparticles.

Due to the close proximity of the C2 and C3 carbons to the particle surface, relaxation effects are expected to broaden the corresponding resonance lines, to decrease the intensity and, in consequence, to complicate the observability of these signals. In order to increase the signal intensity, a ^{13}C DEPTQ spectrum of the gold nanoparticles was recorded (Figure 10). In contrast to the conventional ^{13}C spectrum (Figure 9), an additional C3 peak was detected (C3a at 34.91 ppm, C3b at 34.28 ppm). In earlier studies on ^{13}C-labelled cysteine-functionalised gold nanoparticles, the carbon signal closest to the gold surface (equivalent to C3 in GSH) was split into three signals.[49] This was interpreted as the presence of three different crystallographic sites for cysteine on the gold surface, leading to a different magnetic environment and therefore a different chemical shift. The results shown here suggest that this is also the case for gold nanoparticles with the larger ligand GSH. However, in the case of glutathione, only two different environments were observed instead of three as with cysteine. We want to emphasize that this result was obtained without isotope-enriched ligand molecules due to the high concentration of dispersed and colloidally stable nanoparticles. Furthermore, this conclusion from NMR

spectroscopy is solely based on the different magnetic environment of the glutathione ligand. For a full structural understanding, it would be necessary to analyse the crystallographic nature of the gold surface, e.g. by modelling approaches.

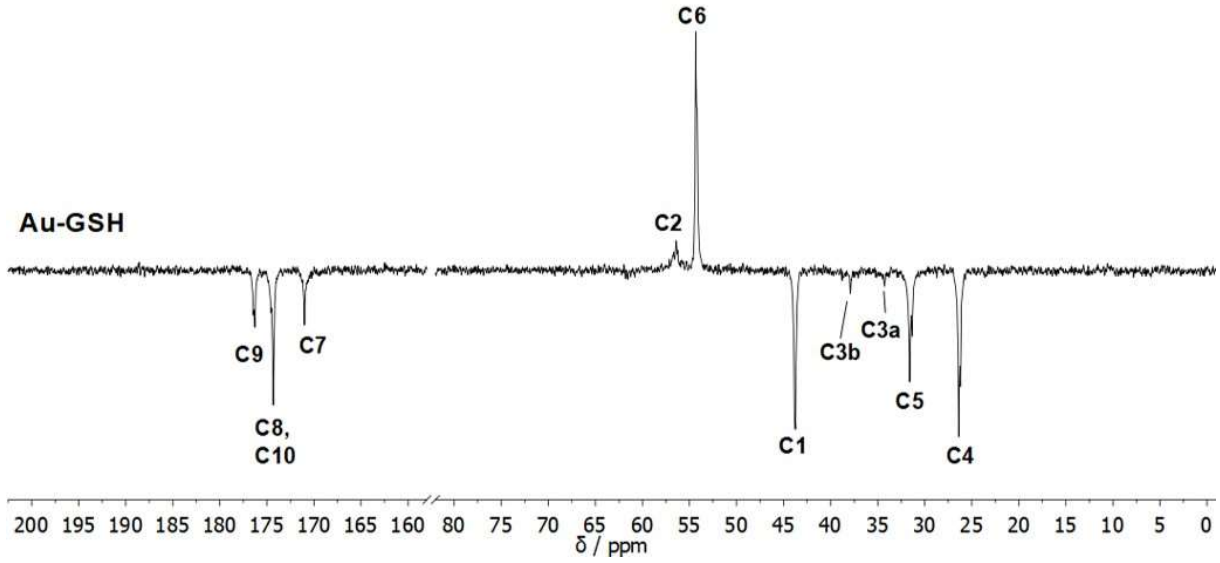

Figure 10: ^{13}C-DEPTQ NMR spectrum of GSH-stabilised gold nanoparticles (100% D_2O; pH 8.5). The signal of carbon atom C3 (next to the gold surface) is split into two signals (C3a, C3b).

In order to confirm the assignments made above, ^{1}H-^{1}H-COSY, ^{1}H-^{13}C-HSQC and HMBC NMR experiments (see Supplementary Information) were performed to elucidate the details of the proton and carbon atom bonding. In all ^{1}H-^{1}H COSY spectra, the couplings of H4/H5 and H5/H6 were observed. The geminal coupling between the diastereotopic H3 protons was seen in the COSY spectrum for the silver nanoparticles, and the coupling of C3-H3 and C2-H2 was seen in the HSQC spectrum. Again, the resolution was strongly reduced in the spectra of platinum and AgPt. In contrast, the physical mixture of silver and platinum nanoparticles showed the same coupling characteristics (H3-H3 in the COSY, C3-H3 and C2-H2 in the HSQC spectrum) as silver nanoparticles.

In the ^{1}H-^{13}C HSQC spectrum of gold nanoparticles (Figure 11), the H3a peaks at 3.46 ppm and 3.33 ppm correlate with C3a at 34.28 ppm; furthermore, the second group of H3b peaks (3.66 ppm; 3.81 ppm) correlates with C3b at 37.91 ppm. In addition, the ^{1}J peak-splitting pattern of H3b/C3b allows to identify the second peak of H3b below the broad peak of H1 and H6. The splitting of the C3a/b and H3a/bsignals confirms the assumption from the ^{13}C-DEPTQ NMR spectrum that the ligand experiences (at least) two different chemical environments on the gold surface. Similarly, in the ^{1}H-^{13}C HSQC spectrum of silver nanoparticles, the coupling of H3a (3.20 ppm; 3.44 ppm) with the C3 atom at 32.69 ppm could be detected. However, due to the lower resolution in the ^{13}C-NMR spectrum and the strong broadening of the ^{13}C signals, a corresponding C3 atom for H3a was not detectable in the ^{13}C spectra. The C3 atom which couples with Hb (3.30 ppm; 3.49 ppm) was detected at 33.40 ppm. These results support earlier indications from silver nanoparticles which were stabilized with ^{13}C-labelled glutathione.[46]

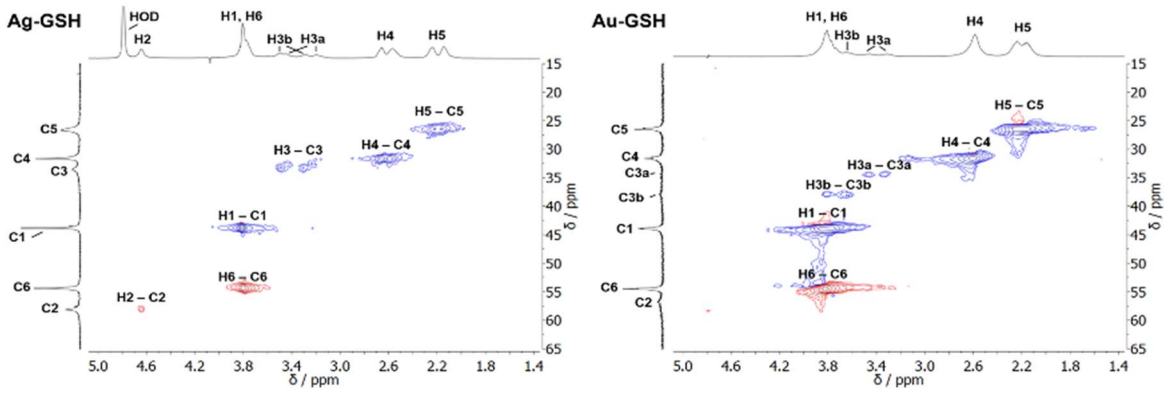

Figure 11: ^{1}H-^{13}C-HSQC NMR spectra of ultrasmall GSH-stabilized nanoparticles (100% D_2O; pH 8.5). For gold nanoparticles, a clear assignment of H3a/C3a and H3b/C3b peaks was possible, indicating two different positions of glutathione on the nanoparticle surface. For silver nanoparticles, the resolution was significantly lower. The colors indicate the different types of carbon atoms as determined by the phase: blue: CH_2; red: CH, CH_3.

^{1}H-^{13}C-HMBC spectra provided further constraints in the structure determination of the ligand shell (Figure 12). In particular, the signals of the carbonyl carbon atoms were unambiguously assigned without supplementary information from the spectrum of dissolved GSH. The HMBC experiment is less sensitive than the HSQC; therefore correlations of ^{1}H resonances with low intensity (such as H3) to neighbouring carbon atoms could not be detected.

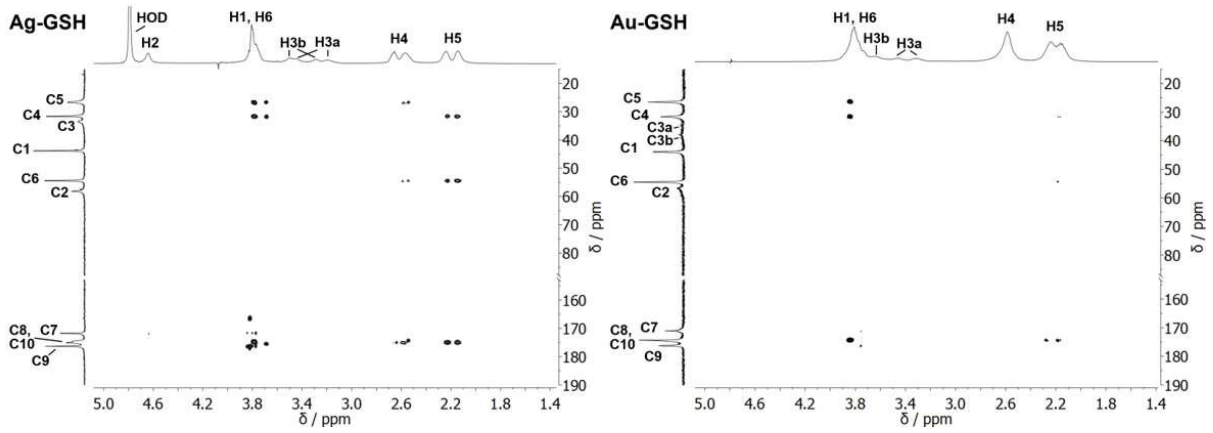

Figure 12: ^{1}H-^{13}C-HMBC NMR spectra of ultrasmall GSH-stabilized nanoparticles (100% D_2O; pH 8.5).

^{1}H-DOSY NMR spectroscopy[67, 68] gave the hydrodynamic diameter of the dispersed nanoparticles.[49, 65, 69, 70] Figure 13 shows the Stejskal-Tanner plots[67] of the ^{1}H-DOSY NMR spectra of all nanoparticles. All nanoparticles diffuse significantly slower (D = $1.28 \cdot 10^{-10}$ to $1.60 \cdot 10^{-10}$ m^2 s^{-1}) than free GSH (D = $4.22 \cdot 10^{-10}$ m^2 s^{-1}), proving that the ligand GSH is attached to the nanoparticles. Based on the obtained diffusion coefficients, the hydrodynamic diameter of the particles was calculated with the Stokes-Einstein equation. Because DOSY yields the hydrodynamic diameter without requiring knowledge about the particle density, these hydrodynamic diameters are larger than those determined by DCS where the hydrodynamic diameter typically is

underestimated by 0.5 to 0.8 nm for ultrasmall GSH-coated nanoparticles.[45, 46] Nevertheless, the hydrodynamic diameters by DOSY are in good agreement with DCS and HRTEM data. Table 3 summarizes all particle characterization data.

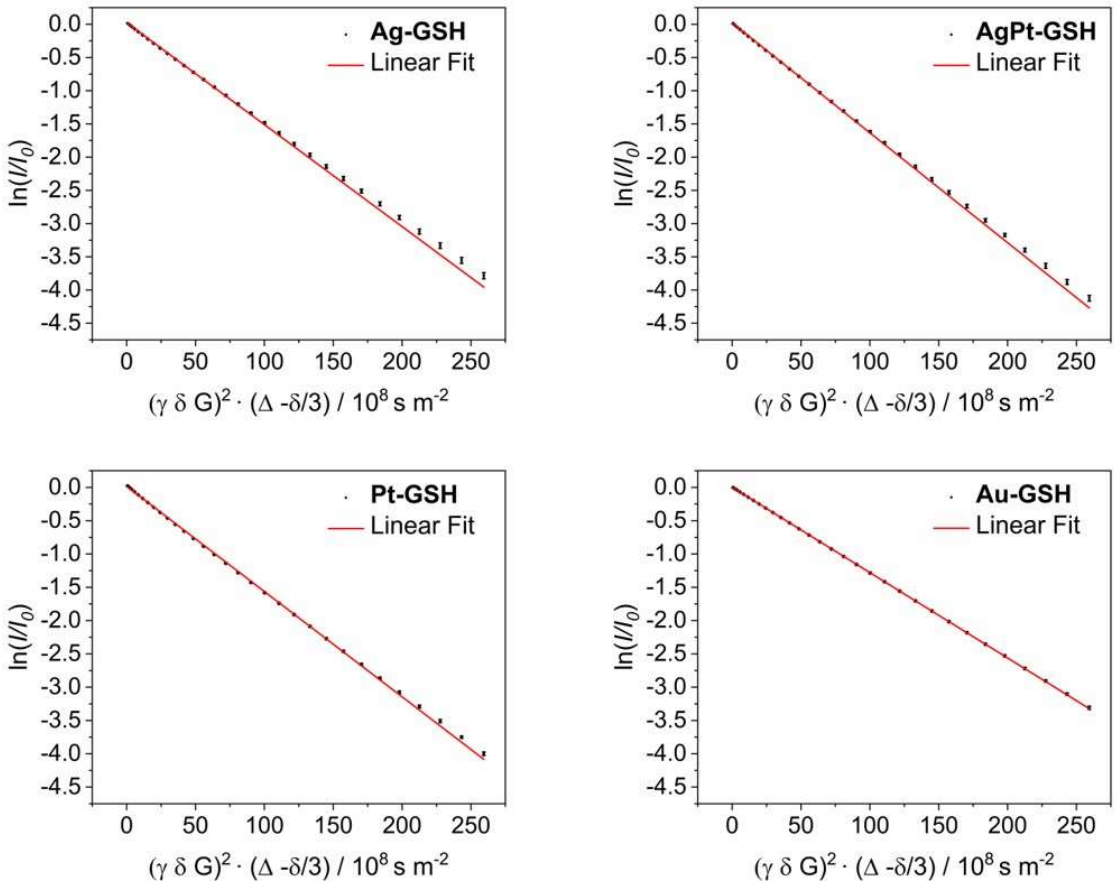

Figure 13: Stejskal-Tanner plots of the ^{1}H-DOSY NMR experiments of GSH-stabilized nanoparticles (10% D_2O, 90% H_2O; pH 8.5). The data points show the average of all analysed ^{1}H signals. Error bars represent the standard deviation of the mean. The translational diffusion coefficient equals the negative slope.

Different methods were used to determine the stoichiometry of the functionalized nanoparticles, i.e. the number of GSH ligands attached to each nanoparticle (Table 3). An average diameter of 2 nm and a spherical shape were assumed. Each particle

contains on average about 250 metal atoms, depending on the metal atom size.[71, 72] For silver, platinum, and gold nanoparticles, the density of the pure metal was used for the calculation. In the case of bimetallic AgPt nanoparticles, the average of the densities of metallic silver and metallic platinum was assumed. First, quantitative ^{1}H-NMR spectroscopy was carried out by adding the reference compound maleic acid at a known concentration. Then, the integrals of maleic acid and of the H5 proton of each kind of nanoparticle were quantitatively compared. Assuming an average nanoparticle diameter of 2 nm with spherical particles and using the measured metal concentration in the dispersion, it was then possible to calculate the nanoparticle concentration in a given dispersion (see ref.[66] for details and examples of the computation steps). Thus, the number of ligands on each nanoparticle can be calculated.

Next, elemental analyses by ICP-MS, AAS/combustion analysis, and EDX were used to determine the sulfur-metal ratio which is indicative for the number of ligands on a nanoparticle with given size (each GSH contains one sulfur atom). Weight percentages were converted into molar percentages and then into molar ratios (Table 3). Overall, the methods agreed well concerning the ratio of metal to sulfur and thus also the number of ligands on the nanoparticles. Of course, each method is associated with its individual error which propagates if the ratio of two error-associated numbers is computed. Thus, the deviation is within the expected range. Figure 14 compares the different quantification methods in terms of the number of ligands per nanoparticle and the resulting footprint. The molecular footprint is normalized to the particle surface and therefore less sensitive to particle size variations.

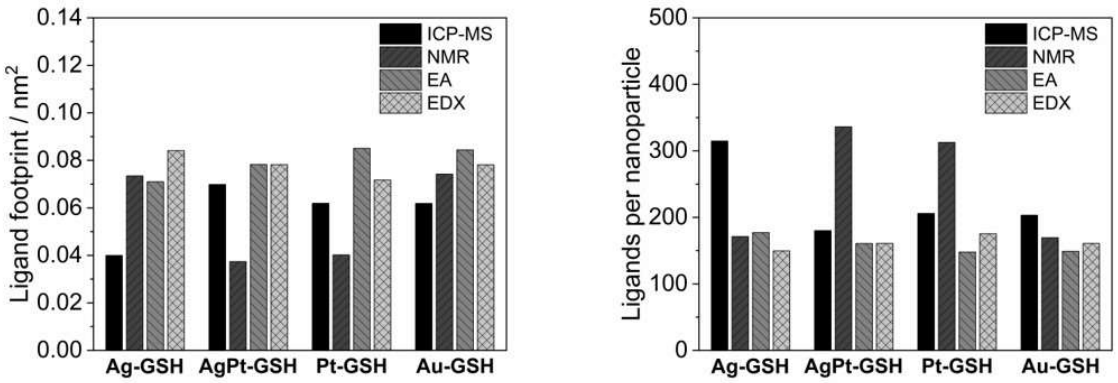

Figure 14: Molecular ligand footprint (**left**) and number of ligands per nanoparticle (**right**) of Ag-GSH, AgPt-GSH, Pt-GSH and Au-GSH nanoparticles as determined by ICP-MS, NMR, elemental analysis (AAS and combustion analysis), and EDX.

Clearly, it is not reasonable to average the results of the four methods, but tentatively, we can say that the particles have approximately the compositions $Ag_{245}GSH_{200}$, $Ag_{130}Pt_{130}GSH_{200}$, $Pt_{277}GSH_{200,}$ and $Au_{247}GSH_{200}$ with an uncertainty of at least ±20% (=±40 GSH) in the number of GSH ligands per nanoparticle. Within the error range, the number of ligands does not depend on the metallic core. The average molecular footprint is 0.063 nm^2 per GSH molecule, again associated with an uncertainty of at least ±20%, i.e. ±0.013 nm^2. The molecular footprint is in good agreement with earlier data on ultrasmall nanoparticles consisting of silver (2 nm; 0.08 nm^2, 150-160 GSH per nanoparticle),[46] gold (2 nm; 0.10 nm^2, 125 GSH per nanoparticle),[66] platinum(II)oxide (1.8 nm; 0.066 nm^2, 153 GSH per nanoparticle),[45] and other platinum metals (1.8 nm; 0.023 to 0.155 nm^2, 66 to 140 GSH per nanoparticle).[45] These ligand numbers appear to be very high at first glance, suggesting a very crowded particle surface, but the results from four independent methods are very consistent. The high curvature of the particle surface clearly contributes to the high surface density.

Table 3: Analytical data of all prepared nanoparticles. The quantification was done assuming an average particle diameter of 2 nm and spherical nanoparticles. [a] The error for DOSY diffusion coefficients and hydrodynamic radii is estimated to be around 20%.

		Ag-GSH	AgPt-GSH	Pt-GSH	Au-GSH
General information	particle core volume / $nm^3 \cdot 10^{27}$	4.19	4.19	4.19	4.19
	particle core weight / $g \cdot 10^{23}$	4.39	6.69	8.98	8.09
	particle density / g cm^{-3}	10.49	15.97	21.45	19.32
	particle core surface area / nm^2	12.57	12.57	12.57	12.57
Particle size	hydrodynamic diameter (DCS) / nm	1.7 ± 0.5	1.6 ± 0.3	1.6 ± 0.4	1.5 ± 0.3
determination	diffusion coefficient (^{1}H-DOSY)[a] /10^{-10} m^2 s^{-1}	1.47	1.60	1.56	1.28
	hydrodynamic diameter (^{1}H-DOSY)[a] /nm	3.32	3.05	3.14	3.81
	particle core diameter (HRTEM) / nm	2.2 ± 0.5	1.8 ± 0.4	2.0 ± 0.4	2.0 ± 0.4
	particle core diameter (HRTEM) / nm	1.0 ± 0.1	1.6 ± 0.1	0.9 ± 0.1	-
ICP-MS	normalized molar ratio metal(s) : sulfur	1.00 (Ag) : 1.28 (S)	0.59 (Ag) : 0.41 (Pt) : 0.68 (S)	1.00 (Pt) : 0.73 (S)	1.00 (Au) : 0.82 (S)
	overall nominal composition of one nanoparticle	$Ag_{245}GSH_{315}$	$Ag_{156}Pt_{110}GSH_{180}$	$Pt_{277}GSH_{206}$	$Au_{247}GSH_{203}$
	GSH molecular footprint / nm^2	0.040	0.070	0.062	0.062
Quantitative NMR: AAS	normalized molar ratio metal(s) : sulfur	1.00 (Ag) : 0.70 (S)	0.54 (Ag) : 0.46 (Pt) : 1.27 (S)	1.00 (Pt) : 1.13 (S)	1.00 (Au) : 0.68 (S)
(Ag, AgPt, Au) and ICP-	overall nominal composition of one nanoparticle	$Ag_{245}GSH_{171}$	$Ag_{143}Pt_{123}GSH_{336}$	$Pt_{277}GSH_{313}$	$Au_{247}GSH_{169}$
MS (Pt)	GSH molecular footprint / nm^2	0.073	0.037	0.040	0.074
Elemental analysis: AAS	normalized molar ratio metal(s) : sulfur	1.00 (Ag) : 0.72 (S)	0.59 (Ag) : 0.41 (Pt) : 0.60 (S)	1.00 (Pt) : 0.53 (S)	1.00 (Au) : 0.60 (S)
(Ag, AgPt, Au) and ICP-	overall nominal composition of one nanoparticle	$Ag_{245}GSH_{177}$	$Ag_{157}Pt_{109}GSH_{161}$	$Pt_{277}GSH_{148}$	$Au_{247}GSH_{149}$
MS (Pt) and combustion	GSH molecular footprint / nm^2	0.071	0.078	0.085	0.084
analysis (S)					
EDX	normalized molar ratio metal(s) : sulfur	1.00 (Ag) : 0.61 (S)	0.45 (Ag) : 0.55 (Pt) : 0.61 (S)	1.00 (Pt) : 0.63 (S)	1.00 (Au) : 0.65 (S)
	overall nominal composition of one nanoparticle	$Ag_{245}GSH_{149}$	$Ag_{119}Pt_{147}GSH_{175}$	$Pt_{277}GSH_{175}$	$Au_{247}GSH_{161}$
	GSH molecular footprint / nm^2	0.084	0.078	0.072	0.078

Conclusions

The synthesis of alloyed ultrasmall nanoparticles of silver and platinum with approximately equimolar elemental ratio is possible by a water-based reduction of the metal ions with $NaBH_4$. These alloyed nanoparticles have the same size and ligand shell of their monometallic counterparts, i.e. silver, platinum, and gold nanoparticles, all with a core diameter of about 2 nm as indicated by transmission electron microscopy (HRTEM) and small-angle X-ray scattering (SAXS). Each nanoparticle carries about 200 glutathione ligands for colloidal stabilization. The ligands are firmly attached as demonstrated by DOSY NMR spectroscopy. The high ligand load can be explained by the high curvature of the nanoparticle, leading to a molecular footprint of about 0.063 nm^2 of each glutathione ligand. However, the internal order of the metal core is clearly different for these particles. Whereas gold, platinum, and silver show the typical diffraction peaks of the fcc lattice, the alloyed nanoparticles are fully amorphous in electron diffraction and X-ray diffraction. Notably, X-ray photoelectron spectroscopy showed that all silver- and platinum-containing nanoparticles were at least partially oxidized to Ag(+I) and Pt(+II), respectively.

The nature of the ligand shell can be conventiently probed by solution NMR spectroscopy, thanks to the high synthesis yield and the good water dispersibility of the nanoparticle samples. By a combination of ^{1}H and ^{13}C NMR spectroscopy, including multi-dimensional COSY, HSQC, and HMBC experiments, the glutathione ligands on the nanoparticle surfaces were analyzed in detail. The binding clearly occurs via the thiol group of the central cysteine. A detailed analysis of the spectra showed that there are at least two different magnetic environments of glutathione, an observation that we ascribe to different crystallographic sites on the nanoparticle surface. Notably, the presence of platinum strongly decreased the resolution of the NMR spectra. This indicates that the kind of metal plays a significant role when it comes to NMR spectra of ultrasmall nanoparticles. However, this effect gives the clear proof that we have

alloyed ultrasmall AgPt nanoparticles as a comparison with a physical mixture of silver and platinum nanoparticles of the same size immediately shows.

Experimental

Chemicals and reagents

As metal precursors, we used silver nitrate ($AgNO_3$, Carl Roth, 99%), hexachloridoplatinum(+IV) acid (H_2PtCl_6, 8 wt% in H_2O; Sigma Aldrich, Steinheim, Germany) and tetrachloridoauric(+III) acid ($HAuCl_4$), which was obtained by dissolution of elemental gold in *aqua regia*. As reducing agent, sodium borohydride ($NaBH_4$, 96%; Sigma-Aldrich) was used. The particles were stabilized with L-glutathione (GSH, 98%; Sigma-Aldrich). Sodium hydroxide (NaOH, 1 M; Bernd Kraft, Duisburg, Germany), hydrochloric acid (HCl, 37%; Bernd Kraft), and nitric acid (HNO_3, 67%; Bernd Kraft) were used. For all syntheses and analyses, ultrapure water (Purelab ultra instrument from ELGA, Celle, Germany) with a specific resistivity of 18.2 MΩ was used unless otherwise noted. Before use, all glassware was cleaned with boiling *aqua regia* and washed twice with water.

All synthesized nanoparticles were stable in aqueous dispersion for at least 4 weeks during storage at 4 °C. There was no indication of agglomeration or change of particle size as indicated by DCS and UV spectroscopy.

Synthesis

For the preparation of Ag-GSH nanoparticles, a modification of the synthesis reported by Wetzel *et al*. was used.[46] A 100 mL round-bottom flask was filled with 30 mL water and degassed with argon for 15 min. Then 33.94 mg silver nitrate (200 µmol, 21.57 mg Ag) and 184.4 mg glutathione (600 µmol) were each dissolved in 1 mL water and added. The white turbid dispersion was stirred at 0 °C for 30 min. 75.7 mg $NaBH_4$ (2 mmol) was dissolved in 1 mL ice-cold water and rapidly added. The clear orange dispersion was warmed to room temperature

and stirred for 1 h whereupon it turned dark red. The nanoparticles were isolated by spin filtration and washed twice with 0.1 M NaOH and six times with water (10 kDa Amicon spin filters at 4000 rpm, 2500 g, 20 min) to remove unbound GSH and synthesis by-products. The yield was about 70% (15 mg) with respect to silver (determined by AAS).

For the synthesis of Pt-GSH nanoparticles, a synthesis reported by Wetzel *et al*. was modified.[45] A 100 mL round-bottom flask was filled with 30 mL water and degassed with argon for 15 min. Then 1.10 mL of a solution of H_2PtCl_6 (c(Pt) = 53.15 g L^{-1}, 300 µmol, 58.53 mg Pt) was added. Next, 91.13 mg glutathione (300 µmol, 1 eq. to Pt) dissolved in 1 mL water was added. To the yellow solution, 0.72 mL HCl (37%) was added to obtain a pH of 2.0. The solution was stirred at room temperature for 1 h. 113.5 mg $NaBH_4$ (3 mmol) were dissolved in 1 mL ice-cold water and added. The clear brown dispersion was stirred for 1 h and turned dark-brown. The nanoparticles were isolated by spin filtration and washed twice with 0.1 M NaOH und six times with water (10 kDa Amicon spin filters at 4000 rpm, 2500 g, 20 min) to remove unbound GSH and synthesis by-products. The yield was about 25% (15 mg) with respect to platinum (determined by ICP-MS).

For the synthesis of bimetallic AgPt-GSH nanoparticles, a 1 L round-bottom flask was filled with 400 mL water. The water was degassed with argon for 15 min. Then 1.2 mL of 200 mM silver nitrate solution (24 µmol, 2.57 mg Ag) and 22.1 mg glutathione (72 µmol) dissolved in 1 mL water were added. The solution was stirred for 30 min. 353 µL H_2PtCl_6 (c(Pt) = 53.15 g L^{-1}, 96 µmol, 18.8 mg Pt) and 30.0 mg glutathione (97 µmol) dissolved in 1 mL water were added and again stirred for 30 min. 113.5 mg $NaBH_4$ (3 mmol) dissolved in 2 mL of ice-cold water was quickly added. The dispersion was stirred for 30 min. The final dispersion was brown. To minimize the volume of water for processing, most of the water was removed in vacuum with a rotary evaporator. The nanoparticles were isolated by spin filtration and washed twice with 0.1 M NaOH und six times with water

(10 kDa Amicon spin filters at 4000 rpm, 2500 g, 20 min) to remove unbound GSH and synthesis by-products. The yield determined by AAS was 68% (1.75 mg, 16.35 μmol) for silver and 15% (2.77 mg, 14.15 μmol) for platinum. By ICP-MS, the yields were 63% (1.61 mg, 15.12 μmol) for silver and 11% (2.01 mg, 10.24 μmol) for platinum. Thus, the particles had a molar ratio of 54 % Ag to 46% Pt as determined by AAS and 59% Ag to 41% Pt as determined by ICP-MS. Note that the ratio of Ag to Pt in the reaction mixture differed from that in the nanoparticles. Silver was incorporated more easily than platinum. The synthesis parameters above were optimized after a series of experiments with variable metal ratios, followed by elemental analysis of the alloyed nanoparticles.

For the synthesis of the Au-GSH nanoparticles, a synthesis reported by Klein *et al.* was modified.[66] A 1 L round-bottom flask was filled with 300 mL of water. The water was degassed with argon for 15 min. Then 4.91 mL of 10.19 g L^{-1} $HAuCl_4$ (254 μmol, 50.0 mg Au,) and 312.2 mg glutathione (1.02 mmol) dissolved in 1 mL water were added and stirred for 15 min. The solution changed its colour from light yellow to light brown and finally became cloudy and white. Then 96.5 mg sodium borohydride (2.55 mmol) was dissolved in 2 mL ice-cold water and added to the solution which was stirred for 20 min. The nanoparticles were isolated by spin filtration and washed twice with 0.1 M NaOH und six times with water (10 kDa Amicon spin filters at 4000 rpm, 2500 g, 20 min) to remove any unbound ligand and synthesis by-products. The yield was about 50% (25 mg) with respect to gold (as determined by AAS).

Electron microscopy

High-resolution transmission electron microscopy (HRTEM) was conducted with an aberration-corrected FEI Titan transmission electron microscope with a Cs-probe corrector (CEOS Company) at a voltage of 300 kV.[73] The nanoparticle dispersion was drop-cast on a copper grid coated with an ultrathin amorphous carbon film, and dried in air at ambient temperature. Fast Fourier transformations

(FFT) of single particle images were performed and analyzed with the program CrysTBox.[74] The sizes of nanoparticles were measured by the program ImageJ.[75]

Energy-dispersive X-ray spectroscopy (EDX)

Energy-dispersive X-ray spectroscopy was performed with an Apreo S LoVac scanning electron microscope (Thermo Fisher Scientific) in combination with a Thermo Scientific UltraDry silicon drift X-ray detector on dried particles on a silicon sample holder.

X-ray powder diffraction (XRD)

XRD was performed with a Bruker D8 Advance powder diffractometer in the Bragg-Brentano reflection mode with Cu Kα radiation (λ = 1.54 Å; 40 kV, 40 mA). Water-dispersed nanoparticles were drop-cast on a silicon single crystal sample holder to minimize scattering and gently dried with a warm air flow to obtain a dense and uniform particle distribution on the sample holder. Each sample was measured from 20 to 90° 2Θ with a step size of 0.02° and a counting time of 8 s, resulting in a total measurement time of 8.4 h per sample. Additionaly, a silicon sample holder alone (without nanoparticles) was measured under the same condition to exclude background scattering (see Supplementary Information, Figure S4). Qualitative phase analysis was performed by Diffrac.Suite EVA V1.2 (Bruker) with the patterns of Ag (#04-0783), Au (#04-0784), Pt (#04-0802), Ag_2O (#41-1104), and PtO (#47-1171) from the ICDD database. Quantitative Rietveld refinement was performed with the software TOPAS 5.0 (Bruker) to calculate phase ratios, lattice parameters and crystallographic densities, as well as the average crystallite size CS from diffraction peak broadening with

$$CS\ (IB) = \frac{\mathrm{K}\cdot\lambda}{IB\cdot\cos} \qquad \text{and} \qquad CS\ (FWHM) = \frac{\mathrm{K}\cdot\lambda}{FWHM\cdot\cos\theta} \qquad (1)$$

where K is a constant set to 0.89 (assuming a spherical particle shape), λ is the wavelength of the X-radiation, IB is the integral breadth of the diffraction peaks in radians (after considering the instrumental peak broadening), and θ is the diffraction angle. The calculation of CS from the full width at half maximum (FWHM) was added for comparison.

Small-angle X-ray scattering (SAXS)

The experimental data were collected at the setup Xenocs-Xeuss 2.0 at the Institute of Physics, University of São Paulo. The instrument is equipped with a Genix3D CuKα (λ = 1.54189 Å) microfocus source, Fox3D mirrors and two sets of scatterless slits. As a result, a parallel beam with cross section size of 0.7·0.7 mm^2 is generated. The 2D scattering data is collected on a Dectris-Pilatus 300k pixel detector. Azimuthal integrations were performed with the program Fit2D,[76] providing 1D curves of the intensity as a function of the reciprocal space momentum transfer modulus q: $q = 4\pi \sin(\theta) / \lambda$, where θ is the scattering angle. The sample to detector distance was 564.7 mm which gives a q range of $0.019 < q < 0.69$ $Å^{-1}$. The liquid samples were placed on home-made reusable sample holders consisting of a thin borosilicate glass capillary with 1.5 mm of diameter glued on stainless steel cases and rubber caps for sealing. Thereby, the holder can be washed and rinsed, allowing the acquisition of the scattering from the sample and blank in the same experimental conditions. Pure water was used as blank for the data treatment and for absolute scale calibration. Data treatment, error calculation and calibration to absolute scale were performed with the program package SUPERSAXS.[77]

The scattering data were modeled with a model based on polydisperse hard spheres. The polydisperse spheres are described by the form factor $P_{poly}(q)$ which is composed of spheres with number distribution expressed by a Schulz-Zimm function with average value R_0, and standard deviation σ. The curves showed a decrease at low angles, indicating a repulsive interaction. A simple hard spheres

interaction $S_{HS}(q)$ with average interaction radius R_{HS} and volume fraction η was used. The final theoretical curve is given by[78, 79]

$$I(q) = Sc_1 P_{poly}(R_0, \sigma, q) S_{HS}(q, R_{HS}, \eta) + \mathrm{BG} \quad (2)$$

where Sc_1 is an overall scale factor, and BG a constant background. Mathematical details are reported in refs.[77-79]

NMR spectroscopy

For quantitative ^{1}H-NMR measurements, 540 µL of water-dispersed nanoparticles (up to 20 mg metal per tube) were mixed with 60 µL of D_2O to obtain a final concentration of 90% water and 10% D_2O. The nanoparticles were freeze-dried and redispersed in 100% D_2O for ^{1}H, ^{13}C, ^{1}H-^{1}H-COSY, ^{1}H-^{13}C-HSQC and HMBC NMR experiments.

^{1}H- and ^{13}C-NMR measurements were performed on a AV HD III spectrometer (BRUKER, Rheinstetten, Germany) equipped with a nitrogen-cooled probe and operating at 600.13 MHz and 150.90 MHz, respectively. ^{1}H-NMR spectra were recorded with excitation sculpting to suppress the ^{1}H signal of the solvent. For the same purpose, presaturation of the water signal was applied in COSY, HSQC, and HMBC experiments.

DOSY-NMR spectroscopy

180 µl of water-dispersed nanoparticles (up to 5 mg metal per tube) were mixed with 20 µl of D_2O to obtain a final composition of 90% water and 10% D_2O. DOSY-NMR spectroscopy was performed with a Bruker Avance III 700 MHz spectrometer with a 5 mm TCI cryoprobe with a *z*-gradient at 25 °C. The ^{1}H-DOSY pulse sequence from the Bruker library was modified with a pre-saturation pulse for water suppression. Spectra were measured with a diffusion time of Δ = 100 ms, and a pulsed gradient duration of δ = 3.5 ms for GSH-coated

nanoparticles. The gradient strength was incremented from 5 to 95% of the maximum gradient strength (66 G cm^{-1} for a smoothed square gradient pulse) in 32 linear steps. Spectra were processed with Topspin 3.7 (Bruker). The linearized diffusion data were plotted and fitted according to the Stejskal-Tanner equation:[67, 68]

$$\ln\left(\frac{I}{I_0}\right) = -\gamma^2 \delta^2 \left(\Delta - \delta/3\right) \cdot D \cdot G^2 \quad (3)$$

with I = signal intensity, I_0 = signal intensity without gradient, γ = gyromagnetic ratio of ^{1}H, δ = diffusion gradient pulse length, Δ = diffusion delay, G = gradient strength, and D = translational diffusion coefficient.

The Stejskal-Tanner plots for three signals of GSH-coated nanoparticles (H1/H6 3.8 ppm, H4 2.5 ppm, 2.2 ppm) were first analysed separately. Upon yielding the same diffusion coefficient within the error margin, the data points of all signals were averaged. Error bars represent the standard deviation of these three proton signals. While the standard error of the Stejskal-Tanner fit itself is small (<2%), we estimate the error for the diffusion coefficient to 20% due to manual integration and potentially overlaying small signals from impurities.

The hydrodynamic diameter was calculated according to the Stokes-Einstein equation:

$$d_H = \frac{k_B \cdot T}{3\pi \cdot \eta \cdot D} \quad (4)$$

with d_H = hydrodynamic diameter, k_B = Boltzmann constant, T = temperature in K, η = dynamic viscosity at 25°C, and D = translational diffusion coefficient.

X-ray photoelectron spectroscopy (XPS)

X-ray photoelectron spectroscopy (XPS) was performed with a spectrometer from SPECS GmbH equipped with a Phoibos 150 1D-DLD hemispherical energy

analyzer. The monochromatized Al Kα X-ray source (E=1486.6 eV) was operated at 15 kV and 200 W. For high-resolution scans, the pass energy was set to 20 eV. The medium area mode was used as lens mode. The base pressure in the analysis chamber was $5 \cdot 10^{-10}$ mbar during the experiment. To account for charging effects, all spectra were referred to C 1s at 284.5 eV.

Elemental analysis (AAS, ICP-MS)

Atomic absorption spectroscopy (AAS) was used to determine Ag, Au, and Pt concentrations of the nanoparticle dispersions with a Thermo Electron M-Series spectrometer (graphite tube furnace; operated according to DIN EN ISO/IEC 17025:2005). For the measurement of Ag, 5 µL of a nanoparticle dispersion was dissolved in concentrated nitric acid (955 µL) and diluted with 3 mL water. For the measurement of Au and Pt, 10 µL of a nanoparticle dispersion was dissolved in *aqua regia* (950 µL) and diluted with 3 mL water. The concentrations of Ag, Au, Pt, and S were determined by inductively-coupled plasma-mass spectrometry (Spectro Model Spectro Arcos after microwave digestion) at Microanalytical Laboratory Kolbe (Fraunhofer Institut Umsicht, Oberhausen).

The mass fraction of sulfur in the nanoparticles was additionally determined with a Euro Vector EURO EA Elemental Analyzer according to DIN EN ISO/IEC 17025:2005.

Differential centrifugal sedimentation (DCS)

Differential centrifugal sedimentation, also known as analytical disc centrifugation, was performed with a CPS Instruments DC 24000 disc centrifuge (24,000 rpm, 29,000 relative centrifugal force; rcf). To obtain a density gradient, different sucrose solutions (8 and 24 wt%) were used. To prevent evaporation, dodecane (0.5 mL) was added as top layer. A dispersion of poly(vinyl chloride) (PVC) latex in water with a defined hydrodynamic diameter of 483 nm from CPS was used for calibration before each measurement. The added nanoparticle

dispersion had a volume of 100 µL. To calculate the hydrodynamic diameter of the monometallic nanoparticles, the densities of elemental silver (10.49 g cm^{-3}), elemental platinum (21.45 g cm^{-3}) and elemental gold (19.32 g cm^{-3}) were used. For the bimetallic nanoparticles, the average density of silver and elemental platinum (15.97 g cm^{-3}) was used.

UV-Vis spectroscopy

UV-Vis spectroscopy was performed with a Genesis 50 instrument (ThermoScientifc) in quartz glass cuvettes from 200 nm to 800 nm (600 µL sample volume). The background correction was carried out with ultrapure water.

Safety statement

No uncommon hazards are noted.

Supplementary Information

In the supplementary information contains the following NMR spectra of GSH-stabilized nanoparticles and unbound GSH: ^{1}H-^{1}H-COSY, ^{1}H-^{13}C-HSQC, and ^{1}H-^{13}C-HMBC. Furthermore, X-ray powder diffractograms of all samples and of the sample holder are given.

Acknowledgements

M.E. and M.H. are grateful to the Deutsche Forschungsgemeinschaft (DFG) for generous funding in the projects EP 22/62-1 and HE 7192/8-1. M.E. and C.L.P.O. are grateful to the German Academic Exchange Service (DAAD) and Fundação Coordenação de Aperfeiçoamento de Pessoal de Nível Superior (CAPES - Finance Code 001) for generous funding of a joint project in the frameword of PROBRAL/PPP. C.L.P.O is grateful for the grant #2016/24531-3, São Paulo Research Foundation (FAPESP). We thank Robin Meya and Beate Römer for

elemental analyses (AAS). Sebastian Leiting (MPI für Kohlenforschung, Mülheim) is acknowledged for XPS measurements.

Data Availability statement

The datasets used or analyzed during the current study are available from the corresponding author on reasonable request.

References

1. Loza, K.; Heggen, M.; Epple, M., Synthesis, structure, properties, and applications of bimetallic nanoparticles of noble metals. *Adv. Funct. Mater.* **2020**, 1909260.
2. Shao, Q.; Wang, P. T.; Huang, X. Q., Opportunities and challenges of interface engineering in bimetallic nanostructure for enhanced electrocatalysis. *Adv. Funct. Mater* **2019,** *29*, 1806419.
3. Zaleska-Medynska, A.; Marchelek, M.; Diak, M.; Grabowska, E., Noble metal-based bimetallic nanoparticles: the effect of the structure on the optical, catalytic and photocatalytic properties. *Adv. Colloid Interface Sci.* **2016,** *229*, 80-107.
4. Kunal, P.; Li, H.; Dewing, B. L.; Zhang, L.; Jarvis, K.; Henkelman, G.; Humphrey, S. M., Microwave-assisted synthesis of Pd_xAu_{100-x} alloy nanoparticles: A combined experimental and theoretical assessment of synthetic and compositional effects upon catalytic reactivity. *ACS Catal.* **2016,** *6*, 4882-4893.
5. Breisch, M.; Grasmik, V.; Loza, K.; Pappert, K.; Rostek, A.; Ziegler, N.; Ludwig, A.; Heggen, M.; Epple, M.; Tiller, J. C.; Schildhauer, T. A.; Koller, M.; Sengstock, C., Bimetallic silver platinum nanoparticles with combined osteo-promotive and antimicrobial activity. *Nanotechnology* **2019,** *30*, 305101.
6. Grasmik, V.; Breisch, M.; Loza, K.; Heggen, M.; Köller, M.; Sengstock, C.; Epple, M., Synthesis and biological characterization of alloyed silver–platinum nanoparticles: from compact core–shell nanoparticles to hollow nanoalloys. *RSC Adv.* **2018,** *8*, 38582-38590.
7. Soler, L.; Casanovas, A.; Ryan, J.; Angurell, I.; Escudero, C.; Pérez-Dieste, V.; Llorca, J., Dynamic reorganization of bimetallic nanoparticles under reaction depending on the support nanoshape: the case of RhPd over ceria nanocubes and nanorods under ethanol steam reforming. *ACS Catal.* **2019,** *9*, 3641-3647.
8. Reichenberger, S.; Marzun, G.; Muhler, M.; Barcikowski, S., Perspective of surfactant-free colloidal nanoparticles in heterogeneous catalysis. *ChemCatChem* **2019,** *11*, 4489-4518.

9. Liao, G. F.; Fang, J. S.; Li, Q.; Li, S. H.; Xu, Z. S.; Fang, B. Z., Ag-Based nanocomposites: synthesis and applications in catalysis. *Nanoscale* **2019,** *11*, 7062-7096.
10. Zhao, J. B.; Jin, R. C., Heterogeneous catalysis by gold and gold-based bimetal nanoclusters. *Nano Today* **2018,** *18*, 86-102.
11. Papaderakis, A.; Mintsouli, I.; Georgieva, J.; Sotiropoulos, S., Electrocatalysts prepared by galvanic replacement. *Catalysts* **2017,** *7*, 34.
12. Luo, M. C.; Guo, S. J., Strain-controlled electrocatalysis on multimetallic nanomaterials. *Nat. Rev. Mater.* **2017,** *2*, 17059.
13. MacArthur, K. E.; Polani, S.; Klingenhof, M.; Gumbiowski, N.; Möller, T.; Paciok, P.; Kang, J.; Epple, M.; Basak, S.; Eichel, R. A.; Strasser, P.; Dunin-Borkowski, R. E.; Heggen, M., Post-synthesis heat treatment of doped PtNi-alloy fuel-cell catalyst nanoparticles studied by in-situ electron microscopy. *ACS Appl. Energy Mater.* **2023,** *6*, 5959-5967.
14. Beermann, V.; Gocyla, M.; Willinger, E.; Rudi, S.; Heggen, M.; Dunin-Borkowski, R. E.; Willinger, M. G.; Strasser, P., Rh-doped Pt–Ni octahedral nanoparticles: understanding the correlation between elemental distribution, oxygen reduction reaction, and shape stability. *Nano Lett.* **2016,** *16*, 1719-1725.
15. Jin, R.; Zeng, C.; Zhou, M.; Chen, Y., Atomically precise colloidal metal nanoclusters and nanoparticles: fundamentals and opportunities. *Chem. Rev.* **2016,** *116*, 10346-10413.
16. Ganguly, M.; Jana, J.; Pal, A.; Pal, T., Synergism of gold and silver invites enhanced fluorescence for practical applications. *RSC Adv.* **2016,** *6*, 17683-17703.
17. Guo, S. J.; Wang, E. K., Functional micro/nanostructures: simple synthesis and application in sensors, fuel cells, and gene delivery. *Acc. Chem. Res.* **2011,** *44*, 491-500.
18. Zarschler, K.; Rocks, L.; Licciardello, N.; Boselli, L.; Polo, E.; Garcia, K. P.; De Cola, L.; Stephan, H.; Dawson, K. A., Ultrasmall inorganic nanoparticles: State-of-the-art and perspectives for biomedical applications. *Nanomedicine* **2016,** *12*, 1663-1701.
19. Sousa, A. A.; Schuck, P.; Hassan, S. A., Biomolecular interactions of ultrasmall metallic nanoparticles and nanoclusters. *Nanoscale Adv.* **2021,** *3*, 2995-3027.
20. Liu, Z. H.; Wu, Z. N.; Yao, Q. F.; Cao, Y. T.; Chai, O. J. H.; Xie, J. P., Correlations between the fundamentals and applications of ultrasmall metal nanoclusters: Recent advances in catalysis and biomedical applications. *Nano Today* **2021,** *36*, 101053.
21. Tang, J.; Shi, H. H.; Ma, G. Y.; Luo, L. P.; Tang, Z. H., Ultrasmall Au and Ag nanoclusters for biomedical applications: A review. *Front. Bioeng. Biotechnol.* **2020,** *8*, 1019.
22. Kang, X.; Li, Y. W.; Zhu, M. Z.; Jin, R. C., Atomically precise alloy nanoclusters: Syntheses, structures, and properties. *Chem. Soc. Rev.* **2020,** *49*, 6443-6514.

23. Du, Y. X.; Sheng, H. T.; Astruc, D.; Zhu, M. Z., Atomically precise noble metal nanoclusters as efficient catalysts: A bridge between structure and properties. *Chem. Rev.* **2020,** *120*, 526-622.
24. Du, X. S.; Jin, R. C., Atomic-precision engineering of metal nanoclusters. *Dalton Trans.* **2020,** *49*, 10701-10707.
25. Wang, S. Z.; Du, J. S. S.; Diercks, N. J.; Zhou, W. J.; Roth, E. W.; Dravid, V. P.; Mirkin, C. A., Colloidal crystal "alloys". *J. Am. Chem. Soc.* **2019,** *141*, 20443-20450.
26. Kwak, K.; Lee, D., Electrochemistry of atomically precise metal nanoclusters. *Acc. Chem. Res.* **2019,** *52*, 12-22.
27. Yan, J. Z.; Malola, S.; Hu, C. Y.; Peng, J.; Dittrich, B.; Teo, B. K.; Hakkinen, H.; Zheng, L. S.; Zheng, N. F., Co-crystallization of atomically precise metal nanoparticles driven by magic atomic and electronic shells. *Nat. Commun.* **2018,** *9*, 3357.
28. Zhang, X.; Shastry, S.; Bradforth, S. E.; Nadeau, J. L., Nuclear uptake of ultrasmall gold-doxorubicin conjugates imaged by fluorescence lifetime imaging microscopy (FLIM) and electron microscopy. *Nanoscale* **2015,** *7*, 240-251.
29. Huo, S.; Jin, S.; Ma, X.; Xue, X.; Yang, K.; Kumar, A.; Wang, P. C.; Zhang, J.; Hu, Z.; Liang, X. J., Ultrasmall gold nanoparticles as carriers for nucleus-based gene therapy due to size-dependent nuclear entry. *ACS Nano* **2014,** *8*, 5852-5862.
30. Sokolova, V.; Mekky, G.; van der Meer, S. B.; Seeds, M. C.; Atala, A. J.; Epple, M., Transport of ultrasmall gold nanoparticles (2 nm) across the blood-brain barrier in a six-cell brain spheroid model. *Sci. Rep.* **2020,** *10*, 18033.
31. Boselli, L.; Polo, E.; Castagnola, V.; Dawson, K. A., Regimes of biomolecular ultrasmall nanoparticle interactions. *Angew. Chem. Int. Ed.* **2017,** *56*, 4215-4218.
32. Das, R.; Landis, R. F.; Tonga, G. Y.; Cao-Milan, R.; Luther, D. C.; Rotello, V. M., Control of intra- versus extracellular bioorthogonal catalysis using surface-engineered nanozymes. *ACS Nano* **2019,** *13*, 229-235.
33. Scaletti, F.; Hardie, J.; Lee, Y. W.; Luther, D. C.; Ray, M.; Rotello, V. M., Protein delivery into cells using inorganic nanoparticle-protein supramolecular assemblies. *Chem. Soc. Rev.* **2018,** *47*, 3421-3432.
34. Muraca, F.; Boselli, L.; Castagnola, V.; Dawson, K. A., Ultrasmall gold nanoparticle cellular uptake: influence of transient bionano interactions. *ACS Appl. Bio. Mater.* **2020,** *3*, 3800-3808.
35. Gupta, A.; Moyano, D. F.; Parnsubsakul, A.; Papadopoulos, A.; Wang, L. S.; Landis, R. F.; Das, R.; Rotello, V. M., Ultrastable and biofunctionalizable gold nanoparticles. *ACS Appl. Mater. Interfaces* **2016,** *8*, 14096-14101.
36. Srinivasulu, Y. G.; Yao, Q. F.; Goswami, N.; Xie, J. P., Interfacial engineering of gold nanoclusters for biomedical applications. *Mater. Horiz.* **2020,** *7*, 2596-2618.
37. Knittel, L. L.; Zhao, H.; Nguyen, A.; Miranda, A.; Schuck, P.; Sousa, A. A., Ultrasmall gold nanoparticles coated with zwitterionic glutathione monoethyl

ester: a model platform for the incorporation of functional peptides. *J. Phys. Chem. B* **2020,** *124*, 3892-3902.
38. Zeng, C. J., Precision at the nanoscale: On the structure and property evolution of gold nanoclusters. *Pure Appl. Chem.* **2018,** *90*, 1409-1427.
39. Brust, M.; Fink, J.; Bethell, D.; Schiffrin, D. J.; Kiely, C., Synthesis and reactions of functionalised gold nanoparticles. *Chem. Commun.* **1995**, 1655-1656.
40. Liz-Marzan, L. M., Gold nanoparticle research before and after the Brust–Schiffrin method. *Chem. Comm.* **2013,** *49*, 16-18.
41. Ferreira, R. S.; Lira, A. L.; Torquato, R. J. S.; Schuck, P.; Sousa, A. A., Mechanistic insights into ultrasmall gold nanoparticle-protein interactions through measurement of binding kinetics. *J. Phys. Chem. C* **2019,** *123*, 28450-28459.
42. Sousa, A. A.; Hassan, S. A.; Knittel, L. L.; Balbo, A.; Aronova, M. A.; Brown, P. H.; Schuck, P.; Leapman, R. D., Biointeractions of ultrasmall glutathione-coated gold nanoparticles: effect of small size variations. *Nanoscale* **2016,** *8*, 6577-6588.
43. Calborean, A.; Martin, F.; Marconi, D.; Turcu, R.; Kacso, I. E.; Buimaga-Iarinca, L.; Graur, F.; Turcu, I., Adsorption mechanisms of L-glutathione on Au and controlled nano-patterning through Dip Pen Nanolithography. *Mater. Sci. Eng. C-Mater. Biol. Appl.* **2015,** *57*, 171-180.
44. Banerjee, S.; Liu, C. H.; Lee, J. D.; Kovyakh, A.; Grasmik, V.; Prymak, O.; Koenigsmann, C.; Liu, H.; Wang, L.; Abeykoon, A. M. M.; Wong, S. S.; Epple, M.; Murray, C. B.; Billinge, S. J. L., Improved models for metallic nanoparticle cores from atomic pair distribution function (PDF) analysis. *J. Phys. Chem. C* **2018,** *122*, 29498-29506.
45. Wetzel, O.; Prymak, O.; Loza, K.; Gumbiowski, N.; Heggen, M.; Bayer, P.; Beuck, C.; Weidenthaler, C.; Epple, M., Water-based synthesis of ultrasmall nanoparticles of platinum group metal oxides (1.8 nm). *Inorg. Chem.* **2022,** *61*, 5133-5147.
46. Wetzel, O.; Hosseini, S.; Loza, K.; Heggen, M.; Prymak, O.; Bayer, P.; Beuck, C.; Schaller, T.; Niemeyer, F.; Weidenthaler, C.; Epple, M., Metal–ligand interface and internal structure of ultrasmall silver nanoparticles (2 nm). *J. Phys. Chem. B* **2021,** *125*, 5645-5659.
47. Zhou, S.; Zhao, M.; Yang, T. H.; Xia, Y. N., Decahedral nanocrystals of noble metals: Synthesis, characterization, and applications. *Mater. Today* **2019,** *22*, 108-131.
48. Radnik, J.; Mohr, C.; Claus, P., On the origin of binding energy shifts of core levels of supported gold nanoparticles and dependence of pretreatment and material synthesis. *Phys. Chem. Chem. Phys.* **2003,** *5*, 172-177.
49. Ruks, T.; Beuck, C.; Schaller, T.; Niemeyer, F.; Zähres, M.; Loza, K.; Heggen, M.; Hagemann, U.; Mayer, C.; Bayer, P.; Epple, M., Solution NMR spectroscopy with isotope-labelled cysteine (^{13}C, ^{15}N) reveals the surface structure of L-cysteine-coated ultrasmall gold nanoparticles (1.8 nm). *Langmuir* **2019,** *35*, 767-778.

50. Fissan, H.; Ristig, S.; Kaminski, H.; Asbach, C.; Epple, M., Comparison of different characterization methods for nanoparticle dispersions before and after aerosolization. *Anal. Meth.* **2014,** *6*, 7324-7334.
51. Yu, R.; Liz-Marzan, L. M.; Garcia de Abajo, F. J., Universal analytical modeling of plasmonic nanoparticles. *Chem. Soc. Rev.* **2017,** *46*, 6710-6724.
52. Langer, J.; Novikov, S. M.; Liz-Marzan, L. M., Sensing using plasmonic nanostructures and nanoparticles. *Nanotechnology* **2015,** *26*, 322001.
53. Cao, N.; Zhou, H.; Tan, H.; Qi, R.; Chen, J.; Zhang, S.; Xu, J., Turn-on fluorescence detection of cysteine with glutathione protected silver nanoclusters. *Methods Appl. Fluoresc.* **2019,** *7*, 034004.
54. Evanoff Jr, D. D.; Chumanov, G., Synthesis and optical properties of silver nanoparticles and arrays. *ChemPhysChem* **2005,** *6*, 1221-1231.
55. Henglein, A., Colloidal silver nanoparticles: photochemical preparation and interaction with O_2, CCl_4, and some metal ions. *Chem. Mater.* **1998,** *10*, 444-450.
56. Safdar, M.; Ozaslan, M.; Khailany, R. A.; Latif, S.; Junejo, Y.; Saeed, M.; Al-Attar, M. S.; Kanabe, B. O., Synthesis, characterization and applications of a novel platinum-based nanoparticles: Catalytic, antibacterial and cytotoxic studies. *J. Inorg. Organomet. Polym. Mater.* **2020,** *30*, 2430-2439.
57. Nguyen, V. L.; Ohtaki, M.; Ngo, V. N.; Cao, M. T.; Nogami, M., Structure and morphology of platinum nanoparticles with critical new issues of low-and high-index facets. *Adv. Nat. Sci: Nanosci. Nanotechnol.* **2012,** *3*, 025005.
58. Wang, L.; Hasanzadeh Kafshgari, M.; Meunier, M., Optical properties and applications of plasmonic-metal nanoparticles. *Adv. Funct. Mater.* **2020,** *30*, 2005400.
59. Zhang, N.; Han, C.; Xu, Y. J.; Foley Iv, J. J.; Zhang, D.; Codrington, J.; Gray, S. K.; Sun, Y., Near-field dielectric scattering promotes optical absorption by platinum nanoparticles. *Nat. Photonics* **2016,** *10*, 473-482.
60. Amendola, V.; Pilot, R.; Frasconi, M.; Marago, O. M.; Iati, M. A., Surface plasmon resonance in gold nanoparticles: a review. *J. Phys. Condensed Matter* **2017,** *29*, 203002.
61. Guo, C.; Yarger, J. L., Characterizing gold nanoparticles by NMR spectroscopy. *Magn. Reson. Chem.* **2018,** *56*, 1074-1082.
62. van der Meer, S. B.; Seiler, T.; Buchmann, C.; Partalidou, G.; Boden, S.; Loza, K.; Heggen, M.; Linders, J.; Prymak, O.; Oliveira, C. L. P.; Hartmann, L.; Epple, M., Controlling the surface functionalization of ultrasmall gold nanoparticles by sequence-defined macromolecules. *Chem. Eur. J.* **2021,** *27*, 1451-1464.
63. van der Meer, S. B.; Loza, K.; Wey, K.; Heggen, M.; Beuck, C.; Bayer, P.; Epple, M., Click chemistry on the surface of ultrasmall gold nanoparticles (2 nm) for covalent ligand attachment followed by NMR spectroscopy. *Langmuir* **2019,** *35*, 7191-7204.
64. Marbella, L. E.; Millstone, J. E., NMR techniques for noble metal nanoparticles. *Chem. Mater.* **2015,** *27*, 2721-2739.

65. Schuetze, B.; Mayer, C.; Loza, K.; Gocyla, M.; Heggen, M.; Epple, M., Conjugation of thiol-terminated molecules to ultrasmall 2 nm-gold nanoparticles leads to remarkably complex ^{1}H-NMR spectra. *J. Mater. Chem. B* **2016,** *4*, 2179-2189.
66. Klein, K.; Loza, K.; Heggen, M.; Epple, M., An efficient method for covalent surface functionalization of ultrasmall metallic nanoparticles by surface azidation, followed by copper-catalyzed azide-alkyne cycloaddition. *ChemNanoMat* **2021,** *7*, 1330-1339.
67. Stejskal, E. O.; Tanner, J. E., Spin diffusion measurements: Spin echoes in the presence of a time-dependent field gradient. *J. Chem. Phys.* **1965,** *42*, 288.
68. Altieri, A. S.; Hinton, D. P.; Byrd, R. A., Association of biomolecular systems via pulsed-field gradient NMR self-diffusion measurements. *J. Am. Chem. Soc.* **1995,** *117*, 7566-7567.
69. Salassa, G.; Burgi, T., NMR spectroscopy: A potent tool for studying monolayer-protected metal nanoclusters. *Nanoscale Horiz.* **2018,** *3*, 457-463.
70. Salorinne, K.; Lahtinen, T.; Koivisto, J.; Kalenius, E.; Nissinen, M.; Pettersson, M.; Häkkinen, H., Nondestructive size determination of thiol-stabilized gold nanoclusters in solution by diffusion ordered NMR spectroscopy. *Anal. Chem.* **2013,** *85*, 3489-3492.
71. Mingos, D. M. P., *Gold Clusters, Colloids and Nanoparticles I*. Springer: Heidelberg, 2014; Vol. 161.
72. Nützenadel, C.; Züttel, A.; Chartouni, D.; Schmid, G.; Schlapbach, L., Critical size and surface effect of the hydrogen interaction of palladium clusters. *Eur. Phys. J. D* **2000,** *8*, 245-250.
73. Thust, A.; Barthel, J.; Tillmann, K., FEI Titan 80-300 TEM. *J. Large-scale Res. Fac.* **2016,** *2*, A41.
74. Klinger, M., More features, more tools, more CrysTBox. *J. Appl. Cryst.* **2017,** *50*, 1226-1234.
75. Schneider, C. A.; Rasband, W. S.; Eliceiri, K. W., NIH Image to ImageJ: 25 years of image analysis. *Nat. Meth.* **2012,** *9*, 671-675.
76. Hammersley, A. P., FIT2D: a multi-purpose data reduction, analysis and visualization program. *J. Appl. Crystallogr.* **2016,** *49*, 646-652.
77. Oliveira, C. L. P.; Vorup-Jensen, T.; Andersen, C. B. F.; Andersen, G. R.; Pedersen, J. S., Discovering new features of protein complexes structures by small-angle X-ray scattering. In *Applications of Synchrotron Light to Scattering and Diffraction in Materials and Life Sciences*, Gomez, M.; Nogales, A.; Garcia-Gutierrez, M. C.; Ezquerra, T. A., Eds. Springer Berlin Heidelberg: Berlin, Heidelberg, 2009; pp 231-244.
78. Garcia, P. R. A. F.; Loza, K.; Daumann, S.; Grasmik, V.; Pappert, K.; Rostek, A.; Helmlinger, J.; Prymak, O.; Heggen, M.; Epple, M.; Oliveira, C. L. P., Combining small-angle x-ray scattering and x-ray powder diffraction to investigate size, shape and crystallinity of silver, gold and alloyed silver-gold nanoparticles. *Braz. J. Phys.* **2019,** *49*, 183-190.

79. Rostek, A.; Breisch, M.; Loza, K.; Garcia, P. R. A. F.; Oliveira, C. L. P.; Prymak, O.; Heggen, M.; Köller, M.; Sengstock, C.; Epple, M., Wet-chemical synthesis of Pd-Au core-shell nanoparticles (8 nm): From nanostructure to biological properties. *ChemistrySelect* **2018,** *3*, 4994-5001.

TOC graphic and synopsis

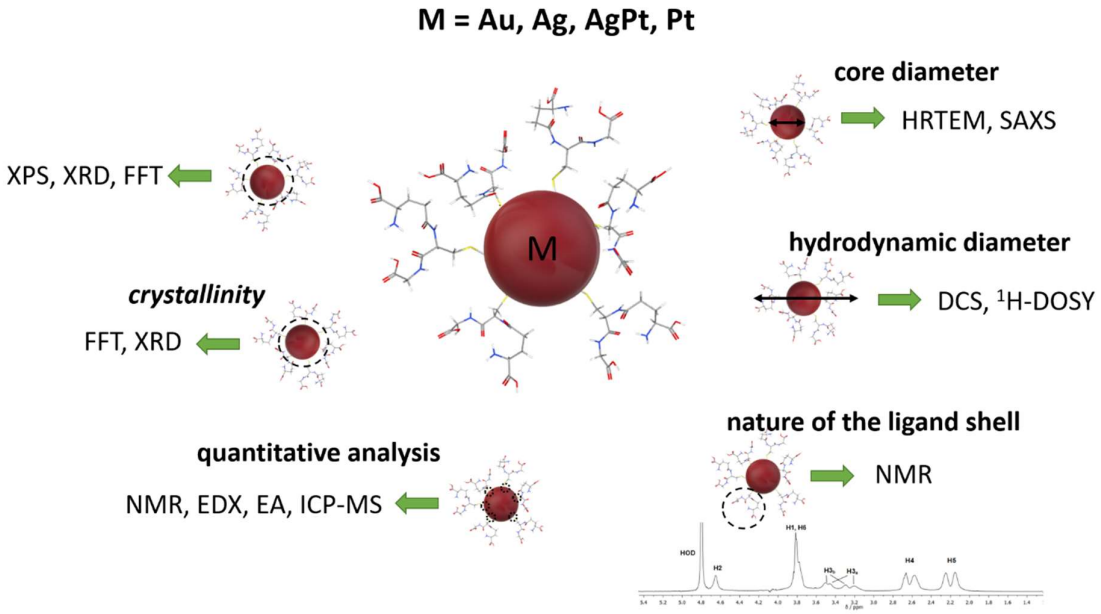

Ultrasmall nanoalloys of silver and platinum with a core diameter of 2 nm were stabilized with a shell of glutathione. A wide range of complementary methods showed their internal structure, e.g. the crystallinity and the metal oxidation state. Notably, the nanoalloys are much more disordered than nanoparticles of the pure metals silver, platinum, and gold. The nature of the glutathione shell was elucidated in detail by extensive NMR studies together with elemental analysis.

Supplementary Information

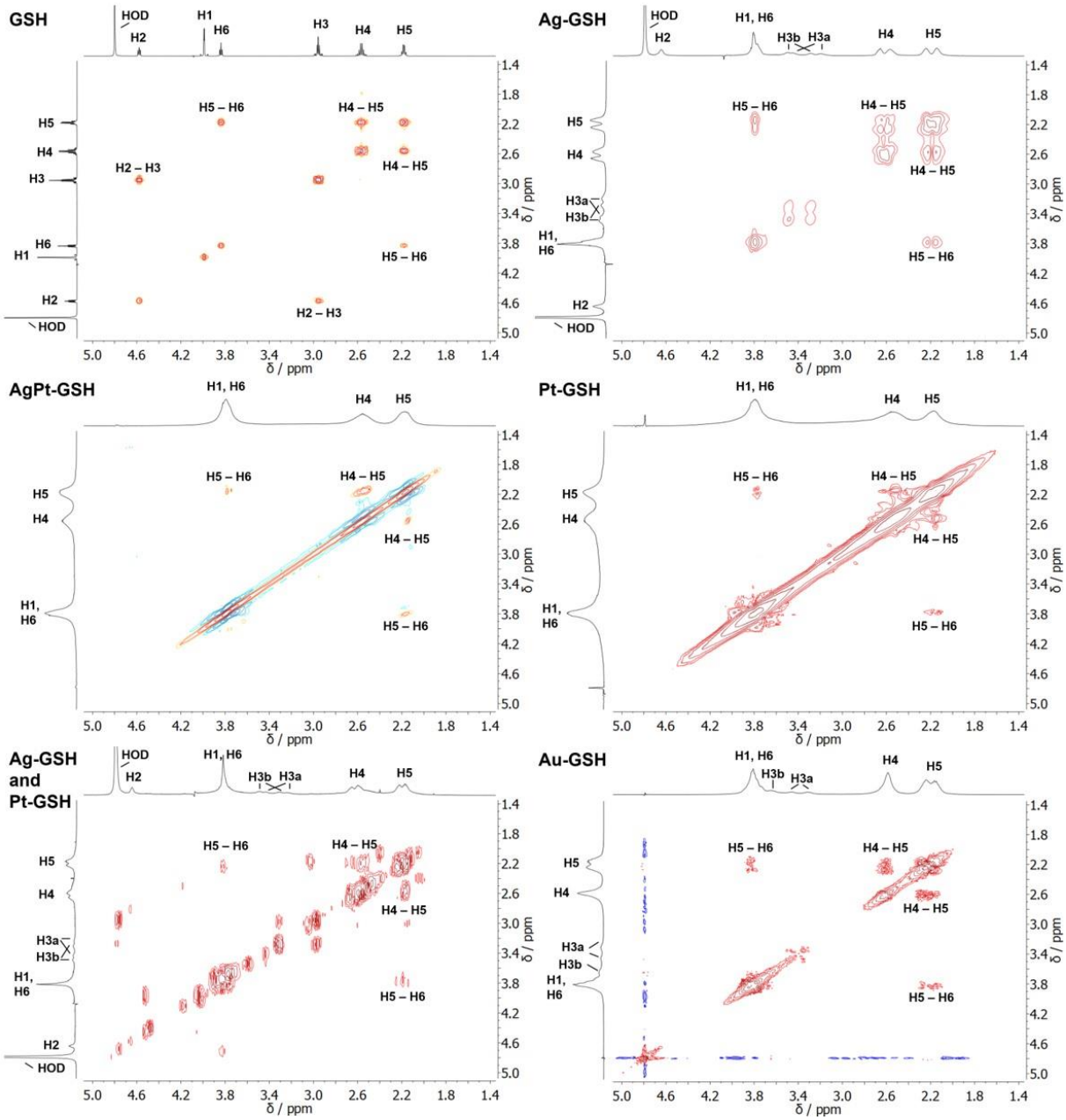

Figure S1: ^{1}H-^{1}H-COSY NMR spectra of GSH-stabilized nanoparticles and unbound GSH (100% D_2O; pH 8.5).

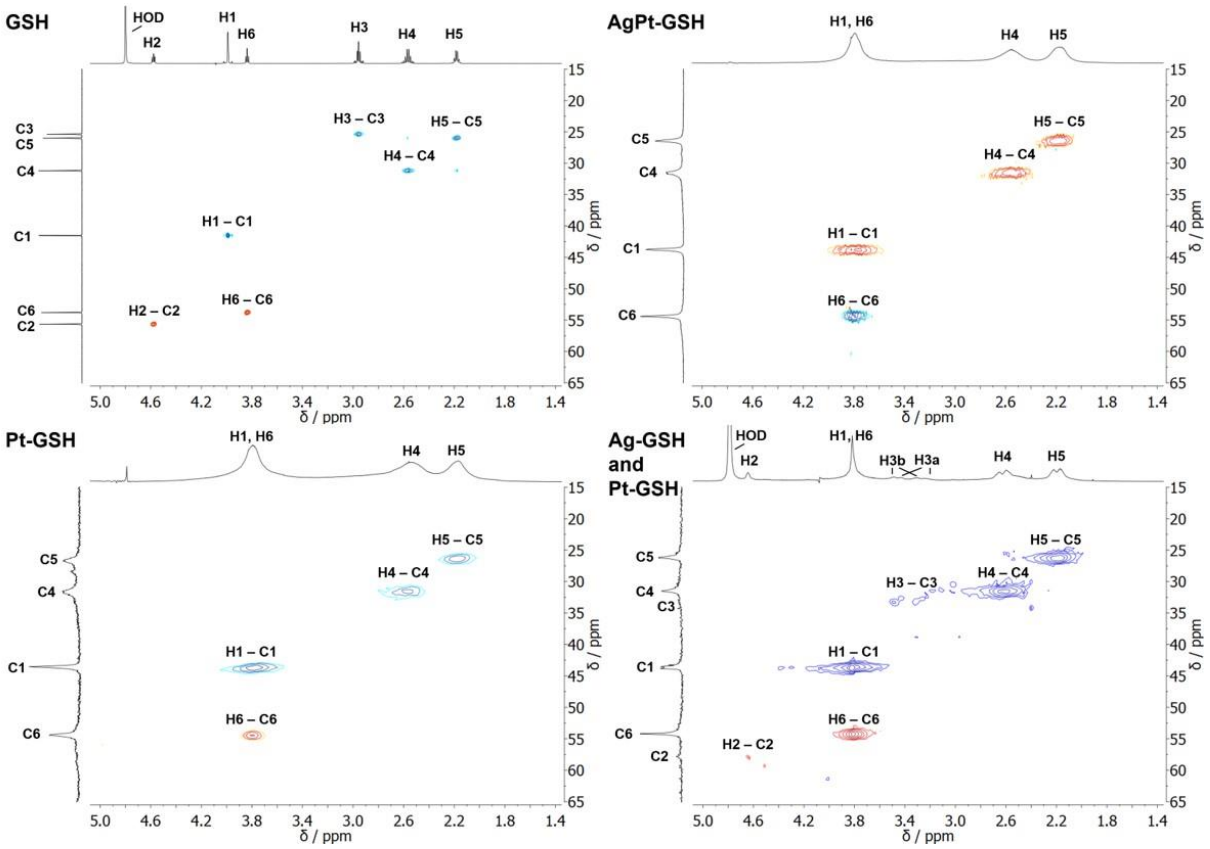

Figure S2: ^{1}H-^{13}C-HSQC NMR spectra of GSH-stabilized nanoparticles and unbound GSH (100% D_2O; pH 8.5). The colors indicate the different types of carbon atoms as determined by the phase: blue: CH_2; red: CH, CH_3.

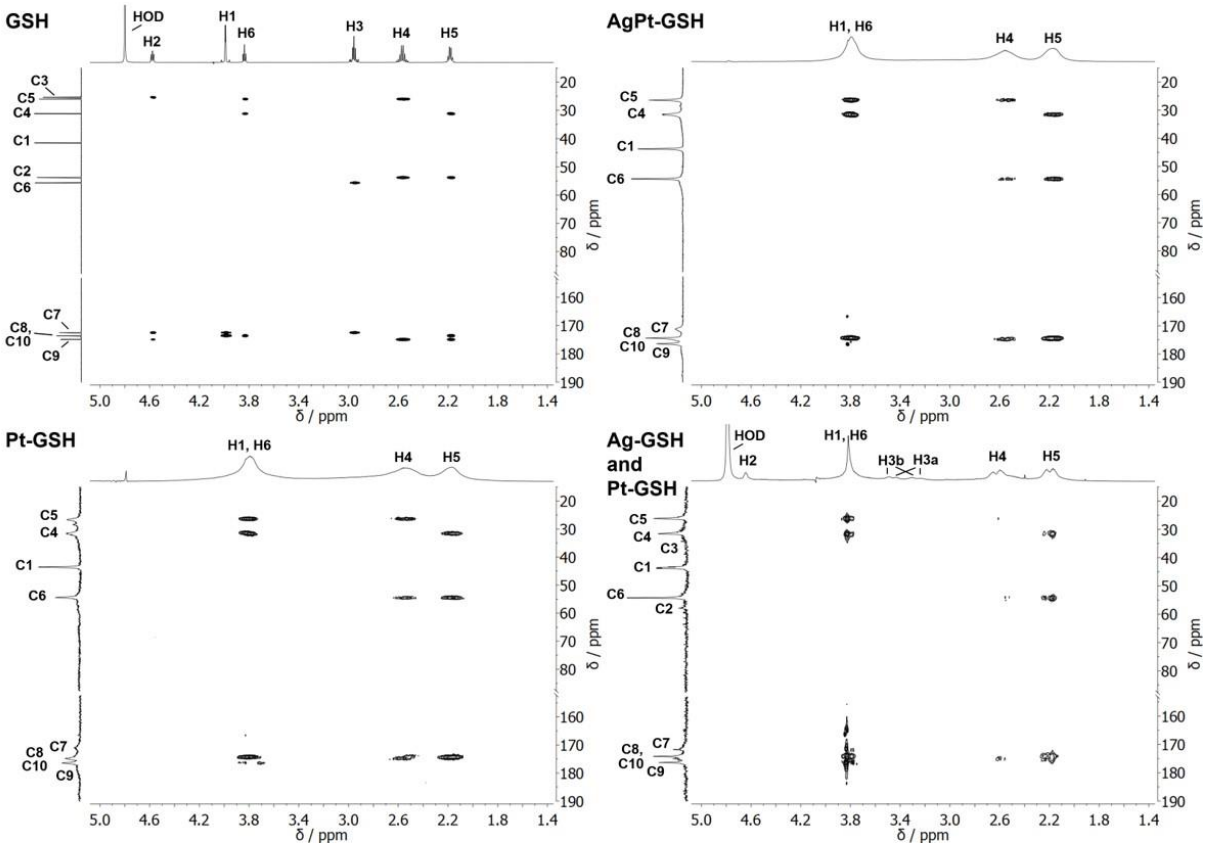

Figure S3: ^{1}H-^{13}C-HMBC NMR spectra of GSH-stabilized nanoparticles and dissolved GSH (100% D_2O; pH 8.5).

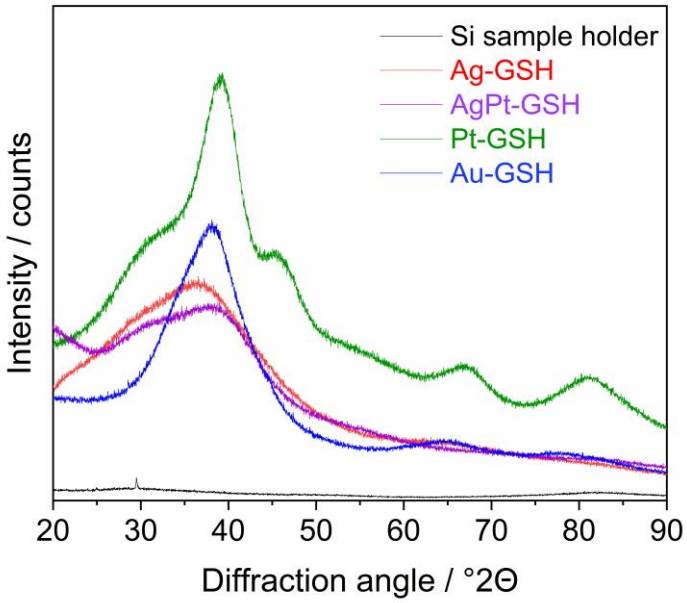

Figure S4: X-ray powder diffractograms of all nanoparticle samples and of the empty silicon sample holder, recorded under the same conditions (counting time, step size). The contribution by the sample holder to the X-ray scattering is negligible.